Exocomets in the β Pictoris system

Klaudia Jaworska

Division of Astrophysics
Department of Physics

LUND
UNIVERSITY

2024–EXA218

Degree project of 15 higher education credits
January 2024

Supervisor: Jens Hoeijmakers

Division of Astrophysics
Department of Physics
Box 118
SE-221 00 Lund
Sweden

Abstract

Comets have been a source of fascination throughout the history of man. In recent years, advances in technology have opened up for the study of extrasolar objects, among them exocomets. The first exocomets were observed in the β Pictoris system almost 50 years ago and the system has been of interest ever since. Still, it is not clearly known where these bodies originate from and how they end up in their star-grazing orbits. In this work, we attempt to answer these questions through N-body simulations of the system. Firstly, the β Pictoris system was simulated with 20 thousand test particles, their position and orbital elements were tracked over an integration length of 20 million years corresponding to the age of the β Pictoris system. Test particles were tracked and many were found to collide, be ejected, or become star-grazing. The results show that there are two regions where possible planetesimal reservoirs could be sustained over the age of the system. It was seen that star-grazers form from the two stable regions at the time scale of the age of the system, which could be an explanation to where exocomets in β Pictoris come from. The majority of star-grazers were found to approach the star at highly eccentric or hyperbolic orbits. Secondly, the identified star-grazers were subjected to simulations including the non-gravitational outgassing force, similar to the one experienced by comets in our own solar system. The simulations show that the outgassing force circularizes the eccentric orbits of test particles. Finally, the mass loss rate was estimated for particles exposed to the non-gravitational force. Kilometer sized exocomets that plunge in from the outer solar system can evaporate on a timescale of a few days as they approach the star within a distance of 0.3 AU

Populärvetenskaplig beskrivning

Kometer har alltid fascinerat människan då de till skillnad från stjärnor och andra objekt på natthimlen rör sig över den. De består av is som frigör gas när kometen kommer tillräckligt nära solen. Gasen ser ut som en svans och ger kometen dess karakteristiska utseende. Förr i tiden saknade människan kunskap om dessa kroppar och de väckte rädsla. Kometer sågs som dåliga omen och tecken på gudarnas ilska. Under 1500-talet började kometer studeras av astronomer. Trots att förståelsen av kometer ökade, avtog inte fascinationen av dem bland såväl allmänhet som forskare, utan håller kvar sig än idag. Kometer tros bära med sig viktig information om begynnelsen av vårt solsystem, som exempelvis ledtrådar om hur livet på jorden kom till.

Detta arbete fokuserar på att undersöka kometer i ett annat solsystem, så kallade exokometer. De är svårare att observera på grund av att de befinner sig väldigt långt bort från jorden. Dock är det både viktigt och relevant att studera exokometer, då de kan hjälpa oss förstå hur andra solsystem formas och därigenom bidra till en bättre förståelse av vårt egna solsystem. Systemet som studeras här heter Beta Pictoris och är det första där exokometer kunnat observeras. Det består av en stjärna, två planeter samt en disk av damm som omger hela systemet. Vi hoppas ta reda på var exokometer som observerats i systemet kommer från och hur de hamnar i extrema omloppsbanor runt sin stjärna.

Vi använder oss av simulationer där vi skapar en modell av Beta Pictoris systemet. Genom simulationerna beräknas gravitationskraften mellan stjärnan och planeterna, så att systemets utveckling genom tid kan studeras. Dessutom inkluderas masslösa test-partiklar i simulationerna och deras rörelse i systemet studerades. Genom detta kan vi se vilka test-partiklar som faller in i stjärnan och blir exokometer. På så sätt hoppas vi kunna dra slutsatser om var exokometerna i systemet kommer från. Förutom detta vill vi se om den kraft som uppstår när exokometen utsöndrar gas har en påverkan på formen av dennes omloppsbana. Vårt syfte är att se ifall kraften kan förklara de extrema omloppsbanorna som exokometerna observeras i.

Acknowledgements

Firstly, I would like to express my gratitude towards my supervisor Jens Hoeijmakers for patience, guidance and support throughout this project. Not only did he provide objective and valuable critique and broadened my analysis, but also inspired and encouraged me to do my absolute best. My thanks go out to Lydia Schollmeier for introducing me to N-body code and discussing my concerns with me. Finally I thank the exoplanet group at Lund Observatory, Bibiana Prinoth, Brian Thorsbro, Nicholas Borsato, Lucian Spitzner, Madeline Lam and Lise Mureau, for encouragement, companionship and advice. Our meetings helped me see the project from new perspectives. Thank you for sharing your knowledge with me.

Contents

Chapter 1

Introduction and Theoretical Background

Comets have fascinated man-kind throughout history however they were first recognized as celestial objects by Tycho Brahe in the sixteenth century. They are thought to carry with them valuable information about the formation of our solar system. Today, astronomy is reaching beyond our own solar system and extrasolar objects have become possible to study with improvements in observational equipment. A lot of attention is turned to exoplanetary systems. This thesis will focus on exocomets in the β Pictoris system, one of the most deeply studied exocometary systems to date.

Exocomets were first observed in the Beta Pictoris (β Pic) system (Beust et al. 1989) as variable features in the spectrum of the star. Recent observations in the form of high-resolution spectroscopy (Kiefer et al. 2014) and precision photometry (Zieba et al. 2019) have shown that exocomets fall into the star at a high rate. It has been shown that these bodies can be on highly eccentric orbits (Kennedy 2018) prior to their infall but it is unclear where they originate from and how they get excited to these infalling trajectories.

In particular, our recent work, see Appendix A, shows the existence of a candidate exocomet in an approximately 15 day orbital period. Via the current project, we wish to use N-body simulations to understand how these objects may migrate from far away in the debris disks to the highly eccentric and short-period orbits which leads to their catastrophic demise as they fall into the star.

1.1 Physics of Orbits

Any massive body will exert a gravitational force on all other bodies. According to Newtons theory, the force between two bodies F decreases as the distance between them increases:

$$F = G\frac{m_1 m_2}{d^2}, \tag{1.1}$$

where m_1 and m_2 are the masses of body 1 and 2 respectively, d is the distance between the bodies and G is the universal gravitational constant. The gravitational force is thus dependent on mass and distance. From Newton's theory of gravitation, Kepler's laws can be derived. According to Kepler's laws, the orbits of planets are elliptical. The position of the star is one of the two focus points of the orbit and the distances where the planet is furthest and closest from its host star are called apoastron and periastron respectively.

An elliptical orbit can be fully described by a set of orbital parameters. Firstly, there is the eccentricity (e). It describes the shape of the ellipse and ranges $0 < e < 1$ for an elliptic orbit. If $e = 0$ the orbit has a fully circular shape and if $e > 1$ the orbit is hyperbolic and is not gravitationally bound to the star its orbiting. Secondly, the semi-major axis (a) is an orbital element that is defined as the longest possible distance between the rim of the ellipse and its center. Another orbital element is the inclination (i), it is defined as the angle between the orbital plane and a reference plane, it can be seen as the tilt of the orbit. The fourth orbital parameter is the longitude of the ascending node (Ω), it is the angle between a reference direction and the orbit's ascending node. The ascending node is the crossing point between the reference plane and the orbital plane. Finally, the last orbital element is the longitude of the periastron (ω), it is the angle between the ascending node and the periastron (Swamy 1997). The orbital elements are illustrated in Figure 1.1.

According to Kepler's third law, for objects in elliptical orbits the period P and semi-major axis a are related as follows:

$$P^2 = \frac{4\pi^2}{G(m_1 + m_2)}a^3, \tag{1.2}$$

where m_1 is the mass of the primary object and m_2 is the mass of the orbiting object (Karttunen et al. 2016). For an elliptical orbit, the distance r from the center is described as:

$$r = \frac{a(1 - e^2)}{1 + e\cos\theta}, \tag{1.3}$$

where θ is the angle between the semi-minor axis and the position of the object in the orbit called the phase shift (Swamy 1997).

Note that the ellipsoidal theory mentioned is an approximation only valid for a system of two bodies. For a gravitational system with three bodies or more there are no analytical solutions to the problem, it can only be solved numerically. N-body simulations focus on simulating the problem of three or more bodies in gravitational interaction with each other in order to find numerical solutions to the N-body problem (Karttunen et al. 2016).

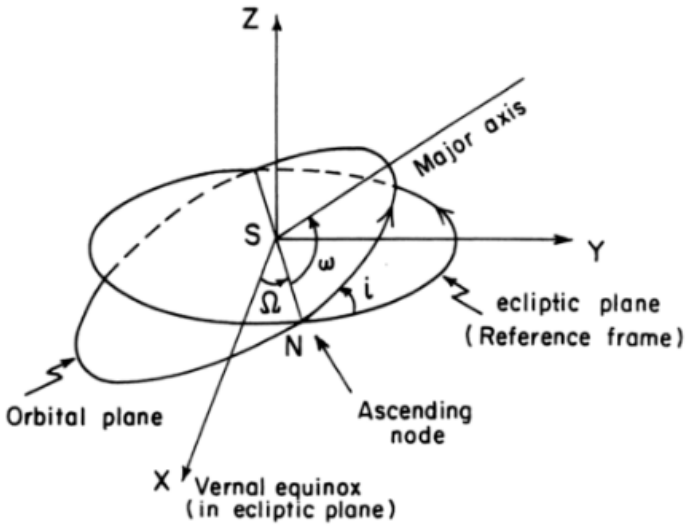

Figure 1.1: The orbital elements illustrated. The star is marked with S. Note that the figure is illustrated with the solar system in mind and the vernal equinox is a reference point on the reference plane. Figure sourced from Swamy (1997).

An object can be trapped by with another object due to its gravitational energy. A particle can be considered trapped by another object if it does not have enough energy to escape its gravitational potential. In case of a 3-body problem of a planet orbiting a much heavier star, the Hill radius approximates the area in which the gravitational force of the planet dominates over the star. If a particle spends significantly long withing the Hill radius of the planet it can be considered trapped. The Hill radius r_{Hill} of a planet in a planetary system can be approximated as:

$$r_{\text{Hill}} \approx a_p^3 \sqrt{\frac{m_p}{3m_S}}, \tag{1.4}$$

where m_p is the mass of the planet, m_S is the mass of the star and a_p is the semi-major axis of the planet (Murray & Dermott 1999).

1.2 Stellar Spectroscopy

Spectroscopy is the study of light by splitting it up into wavelength ranges. Atoms consist of a nucleus surrounded by clouds of electrons. The electrons can change their position in the atomic structure by excitation to a higher electron shell or de-excitation to a lower electron shell. In order for an electron to be excited to a specific level, the exact amount of energy as the potential difference between the two states is required. In contrast, energy is released in the form of radiation when an electron is de-excited. Different electron transitions absorb/release light of different wavelengths (Kitchin 1995).

A spectrum of some light emitting object depicts the flux of light at each specific wavelength range. Thus, it is possible to distinguish if there is a dip or increase in the flux at

a certain wavelength. If the spectrum has a high enough resolution, the change in flux can be traced to an individual electron transition as each electron transition creates absorption or emission lines at specific wavelengths. Through the analysis of stellar spectra the elemental abundances in the star can be found.

1.2.1 Types of Stars

Stars are divided into different classes depending on their luminosity and temperature. The Harvard stellar classification system divides stars into seven main classes denoted with capital letters. The stars are classified based on their temperature. Stellar temperature can be determined from studying temperature sensitive spectral lines in the stellar spectrum. Cool stars are more abundant in neutral elements, the abundance of ionized elements increases with stellar temperature. Lines such as hydrogen Balmer lines, iron lines and ionized calcium lines are often used to determine stellar temperatures.

The spectral sequence ranges from hottest to coolest as follows:

$$\mathrm{O} - \mathrm{B} - \mathrm{A} - \mathrm{F} - \mathrm{G} - \mathrm{K} - \mathrm{M},$$

where spectral class O is the hottest, ranging up to 35 thousand Kelvin and spectral class M is the coolest with temperatures of approximately 3 thousand Kelvin. The spectral classes are often divided into sub-classes denoted by numbers ranging from 0 to 9, where 0 is the coolest and 9 the hottest. As follows from above, A-type stars are among the hottest with temperatures ranging between 7000K to 9000 K. Their spectra are dominated by HI lines for A0 stars. For higher sub-classes neutral metal lines appear in the spectra together with distinct CaII and H lines. See Figure 1.2 for a spectrum of a A6V star, β Pictoris, produced by the High Accuracy Radial Velocity Planet Searcher (HARPS) (Mayor et al. 2003).

The spectral classification as described above only takes the stellar temperature into consideration. Stars in the same spectral class can however have different luminosities. In addition to the spectral class, stars are usually also divided into a luminosity class. The classification system is called the Yerkes classification. The six luminosity classes range from the most luminous, I to the main sequence dwarfs, V (Karttunen et al. 2016).

1.2.2 Radial Velocity and Doppler Shift

The velocity of an astronomical object along the line of sight from Earth is called the radial velocity component of the true velocity. If an object would move only tangentially to the Earth it would appear to not have any radial velocity. The absorption and emission lines in the spectrum of such an object would align with the transition wavelengths measured in the lab for different elements. This is rarely the case for stars. Most stars have some radial velocity with respect to the Earth. It means that they are either moving away or moving towards the Earth. The light from stars like these will be Doppler shifted, meaning that the wavelength will change. If the star is moving towards the Earth its light

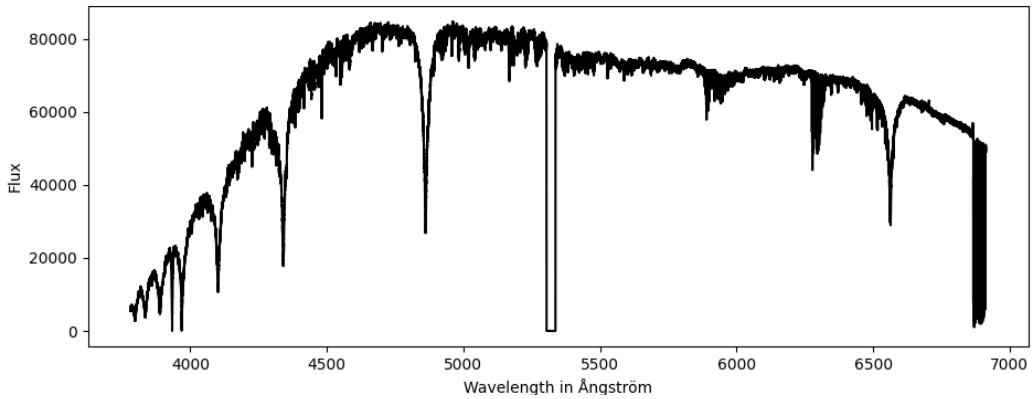

Figure 1.2: Stellar spectrum of β Pictoris, an A6V star, produced by the HARPS spectrograph (Mayor et al. 2003).

will be blue-shifted and if it is moving away from the Earth its light will be red-shifted:

$$\frac{\Delta\lambda}{\lambda_0} = \frac{\lambda - \lambda_0}{\lambda_0} = \frac{v_r}{c}, \tag{1.5}$$

where $\Delta\lambda$ is the change in wavelength, λ_0 is the rest wavelength and λ is the Doppler shifted wavelength such that $\Delta\lambda = \lambda - \lambda_0$. Above v_r is the radial velocity and c is the sped of light. Thus, the spectral lines of a star with some radial velocity will not be at the same wavelengths as expected from laboratory measurements of electron transitions, the Doppler shift needs to be taken into consideration (Kitchin 1995).

When gas moves past the star along the line of sight of an observer, it will absorb some of the stellar light, resulting in absorption lines depending on the dust species. If the gas moves with some velocity relative to the star, the absorption line will appear Doppler shifted on the stellar spectrum with respect to the stellar lines.

1.3 Exoplanet Discovery Methods

Measuring the radial velocity of stars can also be used to detect exoplanets. The radial velocity (RV) method makes use of the fact that a system of two bodies or more rotates around a common center of mass. As the star rotates around the common center of mass, its radial velocity changes, as for about half of its period it moves away from the observer and for the other half it moves toward the observer. The light from the star will be affected due to the Doppler shift, which is periodic for a star hosting a planet and can thus be measured in time-series of spectroscopic observations. In contrast, a single star will have a constant radial velocity. The radial velocity method is appropriate for detection of massive exoplanets with small semi-major axes, as these have a higher impact on the common center of mass and will result in larger radial velocity fluctuations of the host star (Wright 2018).

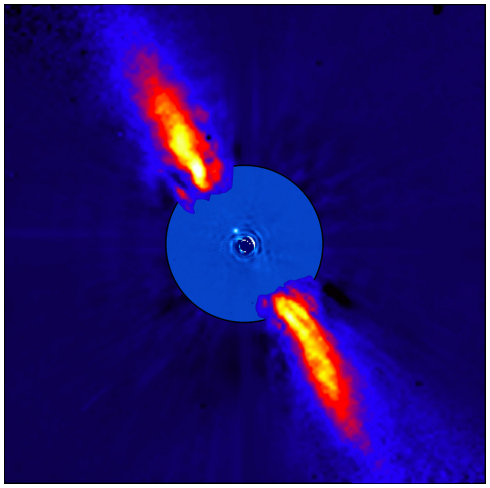

Figure 1.3: The β Pic system imaged in near infra red light. The light of the star has been subtracted and the infra-red light emitted by β Pic b can be distinguished as a bright spot close to the center. The image is a combination of two images, the inner system observed by Lagrange et al. (2009) and the red flares are the debris disk that reflects the stellar light added to the original picture (European Southern Observatory 2008).

To detect exoplanets on very large orbits the direct imaging method can be used. Direct imaging allows for the study of light emitted by the exoplanet itself in contrast to other popular exoplanet detection methods, the transit and radial velocity methods, that instead study the effect of the planet on the light of the host star. The direct imaging method is not dependent on the period of the exoplanet and therefore better suited for detection of exoplanets with long periods. The challenge with direct imaging is the ability to resolve the light emitted by the planet. Planets are located within a small angular distance from their host stars and the signal from the planet is significantly smaller than that of the bright star. The direct imaging method is thus more applicable for detection of exoplanets with large semi-major axes. The light from the star can be subtracted to reveal the planet, it is however complicated to distinguish light from the planet from noise in these observations. The highest planet - to - star signal ratio has been found for hot stars with hot planets in the infra red range of light (Lagrange 2014).

The transit method is the last of the three major exoplanet detection method and it is the method that has been used to detect the most exoplanets. It builds on the fact that as a planet transits the star, meaning that is passes between the star and the observer, it will obstruct a small portion of the stellar light. This dip in the flux can be measured and quantified. The transit method is most efficient for planets with large planetary radius, as they obstruct more of the stellar light. Planets with very long orbital periods are challenging to detect using the transit method, as the probability of transit decreases with increased orbital period. Finally, in order for a planet to transit it must be nearly exactly edge on from the point of view of the observer (Deeg & Alonso 2018).

1.4 Beta Pictoris

β Pictoris (β Pic) is the one of the brightest stars in the Pictor constellation at a distance of 19.28 ± 0.19 pc from Earth, visible from the Southern hemisphere with the naked eye, as it has an apparent magnitude of 3.85 (Crifo et al. 1997). β Pic is estimated to be young, approximately 23 million years old (Mamajek & Bell 2014) and has an effective temperature of approximately 8000 K (Gray et al. 2006). β Pic is located within the β Pictoris moving group of stars, it has been found to be the closest moving group of young stars to the Earth (Mamajek & Bell 2014). A summary of the stellar parameters of β Pic can be found in Table 1.1.

β Pictoris is an interesting system due to several factors. Firstly, as stated before it is a young system. Secondly, the system has been observed to host a large edge-on circumstellar disk (Aumann 1985) making it interesting from a point of view of planetary system evolution. Furthermore, two giant planets have been observed orbiting the β Pictoris star, therefore the system is significant from a planetary science point of view. Finally, falling evaporating bodies (FEB's) or in other words exocomets have been observed in the system opening up for a new way of researching the dynamics and evolution of the system as well as the composition of the material in the disk. See Figure 1.3 for a near infrared image of the system with the stellar light subtracted.

Table 1.1: Stellar parameters of β Pictoris.

Parameter	Value	Reference
Mass	1.73 ± 0.05 $M_\odot$	Lagrange et al. (2009)
Radius	1.7 ± 0.1 $R_\odot$	Crifo et al. (1997)
Spectral Type	A6V	Gray et al. (2006)
Distance from Earth	19.28 ± 0.19 pc	Crifo et al. (1997)
Effective Temperature	8052 K	Gray et al. (2006)
Age	23 ± 3 Myr	Mamajek & Bell (2014)
Apparent magnitude	3.85	Crifo et al. (1997)

1.4.1 The Circumstellar Disk

The β Pictoris system has been a subject of interest ever since the discovery of its circumstellar disk. It was discovered through observation of an excess of infrared light in the proximity of the star, using the Infrared Astronomy Satellite (IRAS). The light was determined to be coming from cold dust orbiting the star (Aumann 1985). The disk is oriented edge-on from the point of view of the Earth (Smith & Terrile 1984).

The circumstellar disk is not a remnant of a protoplanetary disk. It is thought that it has been created due to collisions of large planetesimals (Okamoto et al. 2004). It was found by Okamoto et al. (2004) that the β Pic system has three planetesimal rings feeding the

disk with dust, observed at 6.4, 16 and 30 AU, see Figure 1.4. A fourth planetesimal ring was found in 2011 at a distance of 90 AU from the star (Wilner et al. 2011). N-body simulations of the β Pic system show that there is a stable region in the outer system at approximately 25 AU that could be a potential planetesimal reservoir (Rodet & Lai 2023), see Figure 1.5 . Rodet & Lai (2023) also show that it is highly unlikely that such a reservoir would be able to survive in the inner system of β Pic, because of the gravitational disturbances of the two planets at 2.68 AU and 9.93 AU (Lacour et al. 2021).

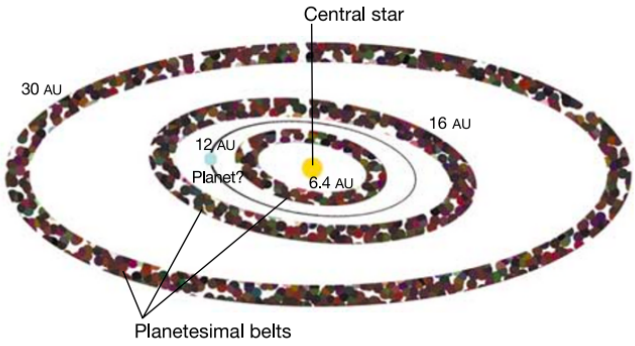

Figure 1.4: The figure presents an illustration of the β Pictoris system done by Okamoto et al. (2004). At the time, no planets were discovered in the system yet, the planet in the figure is a prediction done by Okamoto et al. (2004). Figure sourced from Okamoto et al. (2004).

1.4.2 Planets

The system has been proven to host two gas giants, see Table 1.2 for parameters of the two planets. β Pic b is the outermost planet at a semi-major axis of 9.92 AU (Lacour et al. 2021). It was discovered in infra-red images of the β Pic system, through the high-contrast direct imaging method (Lagrange et al. 2010), see Figure 1.3. β Pic is a young, hot, A-type star and thus a lower fraction of light radiated by them is in the IR regime than for colder stars. Together with the fact that the planets are hot and emit infra red light, this makes the system a prime candidate for direct imaging (Lagrange 2014).

In 2019 a second planet was observed in the system , β Pic c (Lagrange et al. 2019). β Pic c was found at a semi-major axis of 2.68 AU (Lacour et al. 2021), in the habitable zone of the system. β Pic c was discovered trough the RV method. It was not seen on the IR images taken of the system by Lagrange et al. (2010) as it is in the inner part of the stellar system. There have been attempts at observing the planets through the transit method, the slight inclination of the planets is however enough for them to not transit (Kenworthy et al. 2021).

Table 1.2: Planetary parameters of β Pictoris b and c.

Planet	Parameter	Value	Reference
b	Mass	$11.9^{+2.93}_{-3.04}$ M_J	Lacour et al. (2021)
b	Radius	1.65 ± 0.06 R_J	Currie et al. (2013)
b	Semi-major axis	9.93 ± 0.03 AU	Lacour et al. (2021)
b	Eccentricity	0.104 ± 0.003	Lacour et al. (2021)
b	Inclination	$89.0^{+0.01}_{-0.02}$ deg	Lacour et al. (2021)
c	Mass	8.89 ± 0.75 M_J	Lacour et al. (2021)
c	Radius	1.2 ± 0.1 R_J	Nowak et al. (2020)
c	Semi-Major Axis	2.68 ± 0.02 AU	Lacour et al. (2021)
c	Eccentricity	0.32 ± 0.02	Lacour et al. (2021)
c	Inclination	89.95 ± 0.1 deg	Lacour et al. (2021)

1.4.3 Falling Evaporating Bodies

Variable absorption features have been observed in the spectra of the star, interpreted as large falling evaporating bodies (FEBs) or in other words exocomets (Beust et al. 1989). The spectrum of β Pictoris shows absorption features that are wavelength shifted, indicating that they are moving with a velocity with respect to the star and thus are not part of the star itself. These features have mainly been observed at the wavelengths of the Ca II lines at 393.366 and 396.847 nm, and have a variety of profiles (Kiefer et al. 2014), see Figure 1.6 where 8 randomly selected Ca II K profiles from HARPS (Mayor et al. 2003) spectra are plotted. Variable absorptions are also sometimes observed in strong lines of iron, e.g. at 386.0 nm (Welsh & Montgomery 2016).The variable absorption features are interpreted as sublimated material from planetesimals that are grazing the star. No sublimation of volatile materials have been observed in the spectra and thus the exocomets in β Pic are challenging to compare to the comets in our solar system (Fitzsimmons et al. 2023) . Kiefer et al. (2014) conducted an analysis of thousands of stellar spectra and found that the FEBs in the β Pic system can be divided into two families, short lived and long lived comets. They also found the majority of the FEBs to be red-shifted, in agreement with observations done by Beust et al. (1989), meaning that the infalling bodies are indeed on infalling trajectories, and suggesting that such objects do not survive the close passage by the star. The bodies have been determined to be at distances of approximately 0.3 AU when observed and were found to be about kilometer sized (Beust & Morbidelli 2000).

Rodet & Lai (2023) have performed N-body simulations on a three-body system inspired by β Pictoris with the aim to understand the origin of the FEBs. They placed 1000 test particles in orbits of an uniform semi-major axis distribution between 1 and 30 AU. The orbits of the test particles had an uniform distribution of eccentricities between 0 and 0.05, longitude of the node and mean anomaly randomly distributed between 0 and 360°,

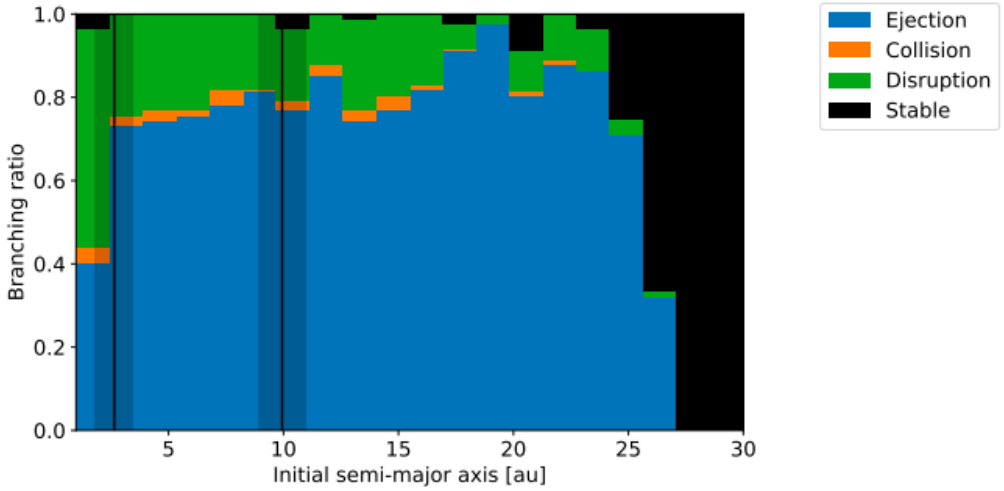

Figure 1.5: Results form the N-body simulations performed by Rodet & Lai (2023) conducted over 10 million years of a three body system inspired by β Pictoris and 1000 test particles. In the figure, disruption is equivalent to star-grazing.

as well as inclinations between 0 and 2° following a cosine prior with respect to the orbital plane of the planets. In their study they find that test particles with initial semi-major axes of between 1-25 AU are mostly either ejected, collide with one of the planets or become star-grazers, see Figure 1.5. The ejection and collision rates decrease for higher initial semi-major axes and the region beyond 25 AU seems to be stable. Star-grazing particles are produced from the region just beyond 25 AU but less so from regions further away

The N-body simulations performed by Rodet & Lai (2023) find a rate of approximately five thousand star-grazing planetesimals per year which is in agreement with FEB observations of the system (Beust & Morbidelli 1996). The results presented by Rodet & Lai (2023) show that particles typically star-graze at the timescale of tens to hundreds of thousands of years. No star-grazers are predicted on the time scale of millions of years, yet the system is approximately 20 million years old (Mamajek & Bell 2014).

This work will aim to reproduce the simulations done by Rodet & Lai (2023) with better precision. The β Pictoris system will be simulated using a larger amount of test particles and over the full lifetime of the system, 20 million years. We aim to trace the movement of test particles in order to draw clearer conclusions on how they become star-grazers and where in the system stable regions are possible.

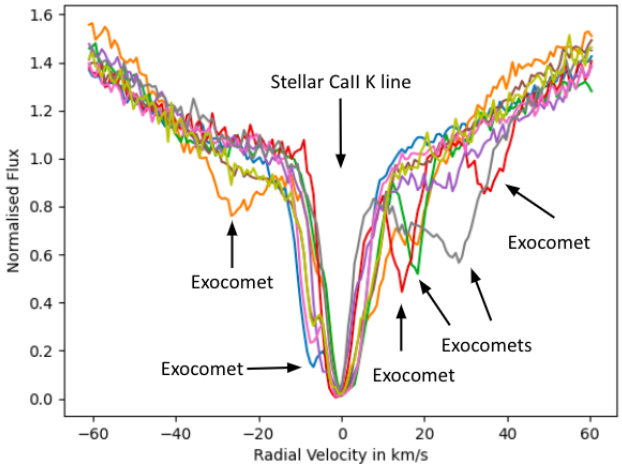

Figure 1.6: Eight HARPS (Mayor et al. 2003) spectra centered at the Ca II K line corresponding to 0 km/s. Other, Doppler shifted absorption features are visible at some radial velocities $|v_r| > 0$. The shifted absorption features do not appear in all the spectra and are thus variable, inferred to be caused by gas from exocomets obscuring the star.

1.5 Comets and Outgassing

Comets are small bodies consisting of an icy nucleus. Due to their eccentric orbits, comets spend most of their time in the colder parts of their orbits. However, as they approach the star its radiation causes material in the nucleus of the comet to sublimate, creating a gaseous cloud around it called the coma. As the comet approaches the star, the coma grows in size and eventually the tails, a dust tail and an ion tail, form as the sublimated material is slower than the nucleus of the comet. Cometary nuclei can through the sublimation lose all icy material such as water and are then considered asteroids. They can continue sublimation of rocky materials which requires higher temperatures, such outgassing asteroids are called active asteroids (Swamy 1997).

The equilibrium temperature T_{eq} of an object at some distance r from a star can be calculated using:

$$T_{\mathrm{eq}} = T_{\mathrm{S}} \left(1 - A\right)^{(1/4)} \sqrt{\frac{R_{\mathrm{S}}}{2r}}, \tag{1.6}$$

where T_{S} is the effective surface temperature of the star, R_{S} is the radius of the star and A is the albedo of the object. The albedo is a measure of the objects ability to reflect light from its surface. For objects with no atmosphere the albedo is often approximated to 0 meaning that they are assumed to absorb all the light that hits their surface (Quirrenbach 2022).

In addition to gravitational forces, star-grazing comets also experience non-gravitational forces from the mass loss resulting from the sublimation, the comet is outgassing. These forces give rise to a non-gravitational acceleration, a_{NG} of the comet. It has been ex-

pressed by Marsden et al. (1973) as follows:

$$\boldsymbol{a}_{\mathrm{NG}} = g(r)\left(A_1\boldsymbol{t}_r + A_2\boldsymbol{t}_t + A_3\boldsymbol{t}_n\right), \tag{1.7}$$

where A_1, A_2 and A_3 are acceleration constants most often given in the unit AU/day^2. The non-gravitational acceleration is defined with respect to orthogonal unit vectors $\boldsymbol{t}_r$, $\boldsymbol{t}_t$ and $\boldsymbol{t}_n$, where the radial vector $\boldsymbol{t}_r$ is pointing from the star in the direction of the comet, $\boldsymbol{t}_t$ that points in the transversal direction and finally, $\boldsymbol{t}_n$ pointing in the direction of the orbital angular momentum and thus perpendicular to the orbital plane. The empirical activity function $g(r)$ is defined as:

$$g(r) = \alpha\left(\frac{r}{r_0}\right)^{-m}\left(1+\left(\frac{r}{r_0}\right)^{n}\right)^{-k}, \tag{1.8}$$

where r is the heliocentric distance of the comet, α is a normalizing constant such that $g(1\,\mathrm{AU}) = 1$, r_0 is the heliocentric distance at which the ice at the surface of the comet begins to vaporize and the exponents m, n and k are constants. (Marsden et al. 1973) As water ice starts to evaporate at temperatures between 145 K and 170 K (Martin & Livio 2012), r_0 was set by Marsden et al. (1973) to be $r_0 = 2.808$ AU.

N-body simulations take into account only the gravitational force meaning that they are only an approximate solution to the N-body problem. Forces like outgassing are not by default not included in standard N-body programs. In case of comets and asteroids, the outgassing force is prominent and will have an effect on the trajectories of the bodies. The outgassing force might be part of the reason as to why planetesimals on orbits with large semi-major axes end up star-grazing. Thus, in order to fully understand the β Pic system the outgassing force should be included.

1.5.1 Mass Loss

Otgassing is per definition associated with mass loss, as sublimated material leaves the surface of a body. The mass loss of a body over time $\dot{M}$ needed for a specific non-gravitational acceleration can be approximated using:

$$\dot{M} = \frac{M g(r)\sqrt{A_1^2 + A_2^2 + A_3^2}}{\kappa v}, \tag{1.9}$$

where M is the mass of the body at a given time t and κ is a factor that accounts for the degree of collimation (collimation efficiency). The κ factor is ranging between $0 \leq \kappa \leq 1$, where ejection is isotropic if $\kappa = 0$ and fully collimated if $\kappa = 1$ (Hui & Jewitt 2017). The non-gravitational acceleration due to mass loss has been modeled for active asteroids in our solar system by Hui & Jewitt (2017). In their work, they choose $\kappa = 0.8$. They argue that low κ values are unrealistic due to the fact that material is emitted towards the Sun, as the Sun-facing side of the asteroid is exposed to the Sun's radiation.

In Equation (1.9), v is the speed of the ejected material. Assuming that the ejected material is a gas, v can be approximated using the Maxwellian distribution of velocities:

$$v = \sqrt{\frac{8k_{\mathrm{B}}T}{\pi\mu m_{\mathrm{H}}}}, \tag{1.10}$$

where T is the temperature of the gas, m_{H} is the average molecular weight of the water gas, $m_{\mathrm{H}} = 1.67 \cdot 10^{-27}$ kg. Above k_{B} is the Boltzmann constant with the value of $k_{\mathrm{B}} = 1.38 \cdot 10^{-23}$ J/K and $\mu = 18$ is the molecular weight for the water ice (Hui & Jewitt 2017).

Finally, the sublimation rate $\dot{Z}$ of an icy body can be approximated using the equilibrium vapor pressure of water ice. The number of particles leaving the surface of the sublimating body will be equal to the number of surrounidng gas particles hitting the surface, $1/4Nv$, under equilibrium conditions. Assuming equilibrium, the sublimation rate can be approximated as:

$$\dot{Z} = \frac{1}{4} N v = Z g(r), \tag{1.11}$$

where N is the density of the gas, v is the mean Maxwellian velocity of the gas particles and Z is the initial vaporization rate, for water $Z = 1.7 \cdot 10^{18}$ mol/cm^2/sec. Swamy (1997)

Thus, the mass.loss and sublimation rate of an object grazing a star can be constrained using Equation 1.9 if the constants A_1, A_2 and A_3 from Equation 1.7 are known as well as the activity function, see Equation 1.8.

Chapter 2

Method

2.1 N-body Simulations

With the aim to reproduce the results obtained by Rodet & Lai (2023), N-body simulations of the β Pic system were performed using Rebound. Rebound is a multi-purpose N-body code that is designed to be used for the needs of astrophysical research where simulations with collisions often must be dealt with, but it can also be used to simulate gravitational systems where collisions do not happen. Rebound enables viewing the evolution of a gravitational system over time. It uses Newton's law of universal gravitation, see Equation (1.1), to compute the acceleration of each particle in the simulation. For a particle with index i the acceleration is computed as:

$$\boldsymbol{a_i} = -\sum_{j=0}^{N_{\text{active}}-1} \frac{Gm_j}{\left(r_{ij}^2 + b^2\right)^{3/2}} \mathbf{r}_{ij}, \tag{2.1}$$

where $\boldsymbol{r}_{ij}$ is the distance between particle with index i and particle with index j. G is the gravitational constant m_j is the mass of particle j and b is the gravitational softening constant, by default set to zero. N_{active} is the number of massive particles in the simulation and all particles with index lager than or equal to N_{active} are treated as test particles (Rein & Liu 2012). The integrator used in the simulations performed was the default Integrator with Adaptive Step-size control, 15th order (IAS15). It is an integrator that can handle conservative and non-conservative forces. It can handle both close encounters between particles as well as particles on highly eccentric orbits (Rein & Spiegel 2015). It is thus good choice for simulating comet-like objects.

The simulations were set-up using the stellar radius and mass from Table 1.1 as well as planetary parameters found in Table 1.2. The planets positions were initialized at the coordinates $(a_p, 0, 0)$, where a_p is the semi-major axis of the planet, see Figure 2.1. Test particles with zero mass were placed on circular orbits with a uniform, random distribution of phase-shifts between 0° and 360°, semi-major axes between 1 and 35 AU and inclinations between 80° and 100°, where 90° is the reference plane. See Figure 2.1 for an example simulation set-up.

When setting up the simulations, it was assumed that the mass of comets is significantly smaller than the mass of both the star and the planets, it was thus assumed to be zero. The assumption of only three massive bodies in the system meant that only the star and the two planets had any gravitational impact on the system while the other particles were test particles, affected by the massive bodies without exerting any gravitational force themselves. This allowed for a quicker integration time. Since the test particles were mass-less they did not in any way affect each other, meaning that the particles could be simulated individually. This allowed for parallelization of the code, so that several simulations containing a smaller amount of particles could be run on several computing cores at the same time shortening the total computing time by a factor of the number of working cores.

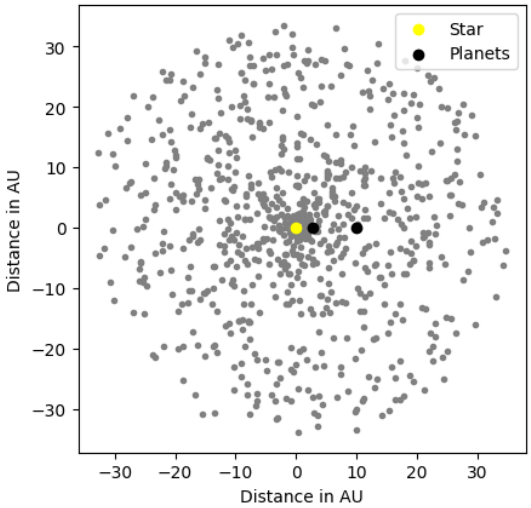

Figure 2.1: An example of the set-up of the simulations run. In the figure the initial positions of star and the planets are included, as well as 1200 test particles. The star is placed at the origin.

After setting up the system similarly to Figure 2.1, the simulation was integrated over time and the positions of all the particles were tracked. Test particles were removed from the simulation when they fulfilled the conditions for collision or ejection. Collision was defined as whenever a test particle's position is recorded within the radius of one of the planets. The positions of the particles were checked every time step, and a straight line was assumed between those positions to lessen the risk of collisions that happen between between two time steps being missed. It was also documented which planet the test particle collided with, giving more fine-grained information about the evolution of particles than what was reported by Rodet & Lai (2023).

A test particle was considered as ejected when it was beyond 150 AU from the star and it had en eccentricity of $e \geq 1$, thus being on a hyperbolic orbit and no longer gravitationally bound to the system. The eccentricity was checked in addition to the distance as some test particles could end up on large, highly eccentric orbits and pass the distance limit, however still be on an elliptic orbit and would eventually come back

into the inner system.

Star-grazing test particles were identified as particles that had a position that was closer than 0.3 AU from the star. This limit is grounded in work done by Beust & Morbidelli (2000) where they argue that the furthest distance from the star that FEBs observed are observed at through variable metal absorption is approximately 0.3 AU. The star-grazing particles were removed and their semi-major axis, eccentricity, phase shift and inclination at the time of removal were saved together with the simulation time. With this information the simulation could be resumed and the three massive bodies, star and planets, would be in the same positions as when the test particle was star-grazing.

The test particles that did not collide with any of the planets, did not get ejected and did not star-graze were considered as stable. The positions of the test particles were also saved for every time-step to determine whether a test particle did not only survive the simulation, but their orbital semi-major axis did not change by more than 5% over the course of the entire simulation. Particles that fulfilled that criterion were labeled as hard stable. The rest of the surviving particles were classified as soft stable: meaning, particles that remain in the system but on very different orbits than those on which they started out.

Furthermore, test particles that captured by one of the planets could be identified by flagging whenever a particle spends a significant amount of time within the Hill radius of said planet, see Equation 1.4. Looking into the capture rates of each planet in more detail may allow for a study of the rate at which the planets accelerate planetesimal debris after the dissipation of the protoplanetary disk, which might be relevant to moon formation; though that this is something outside of the scope of this study.

2.2 Inclusion of Non-Gravitational Acceleration

The outgassing acceleration was defined as in Equation (1.7), with respect to the unit vectors $\boldsymbol{t}_r$, $\boldsymbol{t}_t$ and $\boldsymbol{t}_n$. The coordinate system was set up with the star as the center point, see Figure 2.2. The unit vectors were defined in rebound as follows: $\boldsymbol{t}_r$ is the unit vector in the radial direction, pointing from the star toward the test particle in question. The position coordinates in x, y and z of the test particles are known as they are saved from the simulations done in the previous section. The length and direction of the position vector was found from the position coordinates, using that:

$$R^2 = r_x^2 + r_y^2 + r_z^2, \tag{2.2}$$

where R is the length of the position vector. The position vector was then used to define the radial component of the outgassing acceleration in the x, y and z directions.

For $\boldsymbol{t}_t$, the length and position of the test particle's transversal velocity vector was using that:

$$\boldsymbol{v}_t = r\boldsymbol{v} - \boldsymbol{r}\left(\frac{\boldsymbol{r}\cdot\boldsymbol{v}}{r}\right), \tag{2.3}$$

where $\boldsymbol{v}$ is the orbital velocity vector (Veras et al. 2015).

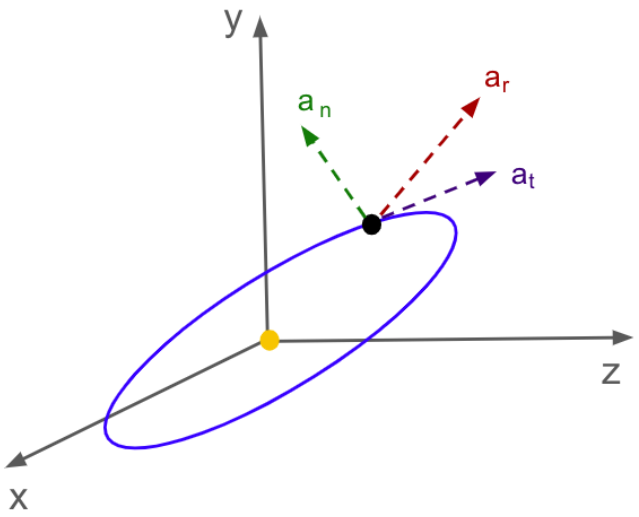

Figure 2.2: The non-gravitational acceleration from Equation (1.7) components visualized in a cartesian coordinate system with the star at the origin.

As for defining $\boldsymbol{t}_n$, the acceleration component orthogonal to the rotation plane, the x, y and z components of the angular momentum were used. In Rebound, the position and velocity coordinates are automatically calculated for each iteration step. This is not the case for the orbital angular momentum. In the case of a circular orbit the position and velocity vectors are orthogonal with each other, this approximation can not be applied to comets. For an elliptic orbit, the following definitions for the components of the angular momentum were used:

$$h_x = r_y v_z - r_z v_y = \pm H \sin i \sin \Omega, \tag{2.4}$$
$$h_y = r_z v_x - r_x v_z = \mp H \sin i \cos \Omega, \tag{2.5}$$
$$h_z = r_x v_y - r_y v_x = H \cos i, \tag{2.6}$$

where i is the orbital inclination and Ω is the longitude of the ascending node, see Figure 1.1. The sign of h_x and h_y changes depending on the inclination, it it is below 90° the top sign is correct and for $i > 90°$ the signs flip to the lower text(Swamy 1997).

Finally, the x,y and z components of $\boldsymbol{t}_r$, $\boldsymbol{t}_t$ and $\boldsymbol{t}_n$ were added together to define the total non-gravitational acceleration in all directions. The equations were the following:

$$a_x = -g(r)\left(A_1 \boldsymbol{t}_r \frac{r_x}{R} + A_2 \boldsymbol{t}_t \frac{v_{t,x}}{H} + A_3 \boldsymbol{t}_n \frac{h_x}{H}\right), \tag{2.7}$$
$$a_y = -g(r)\left(A_1 \boldsymbol{t}_r \frac{r_y}{R} + A_2 \boldsymbol{t}_t \frac{v_{t,y}}{H} + A_3 \boldsymbol{t}_n \frac{h_y}{H}\right), \tag{2.8}$$
$$a_z = -g(r)\left(A_1 \boldsymbol{t}_r \frac{r_z}{R} + A_2 \boldsymbol{t}_t \frac{v_{t,z}}{H} + A_3 \boldsymbol{t}_n \frac{h_z}{H}\right), \tag{2.9}$$

where R and H are the magnitudes of the position vector and angular momentum vector respectively. Similarly, r_i, $v_{t,i}$ and h_i are the coordinates of the position, transversal velocity and orbital angular momentum.

Equation (1.7) is scaled by the activity function from Equation (1.8) which contains constants. The constants were initially determined for comets in the solar system by Marsden et al. (1973). The r_0 parameter was re-scaled to β Pictoris by finding the distance to the star r at which water ice starts to sublimate using Equation (1.6). This temperature was assumed to be 160 ± 20 K, in the range provided by Martin & Livio (2012), note the large error as the value is an assumption since conditions of the system are not known well enough to make a better estimate. Stellar parameters used in the calculation can be found in Table 1.1. The re-scaled constant was found to be $r_{0,\beta Pic} = 10.0 \pm 0.3$ AU. Note that this places both β Pic b and c within the sublimation range for water.

Using Equation (1.8), the constants were set to $k = 0$ and $m = 2$, so that the activity function would decrease as $1/r^2$, as approximated by Micheli et al. (2018) that modeled the non-gravitational acceleration for 'Oumuamua, an object similar to the ones we model. As $k = 0$, the whole second term in Equation (1.8) becomes 1, regardless of the value of n. According to the definition by Marsden et al. (1973), the α constant should be chosen such that the activity function normalizes to 1 at the heliocentric distance of 1 AU. In our solar system, the effective temperature is 278 K at 1 AU, as can be calculated using Equation (1.6). The same temperature is reached at a distance of 3.3 ± 0.2 AU for the β Pictoris system. Thus, α was changed so that the function would normalize to $g(3.3\,\mathrm{AU}) = 1$, which corresponds to $\alpha = 0.11 \pm 0.01$.

The constants A_1, A_2 and A_3 from Equation 1.7 are for comets and active asteroids in the solar system usually determined using observational data. Equation 1.7 is fit to observations of a comet's trajectory where the A-constants are free parameters. Such a study of active asteroids in our solar system has been performed by Hui & Jewitt (2017), where they present the results of fitting A_1, A_2 and A_3 to the trajectories of active asteroids. The values of the magnitude of the A-constants is largely different between different asteroids, ranging form negative 10^{-6} AU/day^2 to positive 10^{-6} AU/day^2. While there is a possibility that the outgassing force acts in the negative direction for a portion of the bodies in the β Pic system, we are interested in how bodies end up on highly eccentric orbits of low orbital periods and thus are interested in the positive direction of the outgassing force. The average value of the positive constants presented by Hui & Jewitt (2017) was determined to be on the scale of 10^{-7} AU/day^2.

Firstly, simulations where only the star and a test particle on an arbitrary orbit were initialized. The outgassing force was then applied as in Equations 2.7. The planets were initially left out in order to disregard their gravitational pull on the test particle and examine how the outgassing force alone affects the particles orbit. The semi-major axis was set to $a = 0.5$ AU and eccentricity of the test particle was changed between 0, 0.2 and 0.9. The strength of the outgassing force was set to $A_1 = A_2 = A_3 = 1 \cdot 10^{-7}$ AU/day^2.

Then, the planets were included and simulations were set up similarly as in Section

2.1, however at first no test particles were added. The system of the three massive bodies was integrated to a time at which a test particle from simulations described in Section 2.1 became star-grazing. Then the test particle itself was added to the simulation and an outgassing force was applied to it. The trajectory and orbital elements of the test particle were tracked. For these simulations, three test particles with different sets of initial orbital parameters, representative of the star-grazing population, were selected based on the results from N-body simulations described in Section 2.1. The initial orbital parameters of the first test particle were: $e_{\mathrm{P1}} = 0.63$, $a_{\mathrm{P1}} = 0.64$ AU and $i_{\mathrm{P1}} = 0.21$ rad. The second set of simulations was performed with particle 2 on an orbit with the following orbital parameters: $e_{\mathrm{P2}} = 0.91$, $a_{\mathrm{P2}} = 0.44$ AU and $i_{\mathrm{P2}} = 0.14$ rad. Lastly particle 3, on an initially hyperbolic orbit, was included as a large portion of all star-grazers were found to be on hyperbolic orbits. The orbital parameters of the third test particle in the final set of simulations was: $e_{\mathrm{P3}} = 1.25$, $a_{\mathrm{P3}} = -1.36$ AU and $i_{\mathrm{P3}} = 0.27$ rad.

The strength applied was varied as : $1 \cdot 10^{-7} < A_i < 1 \cdot 10^{-6}$ AU/day^2, where $i = 1, 2, 3$, which is in the range of what Hui & Jewitt (2017), we chose to also scan larger values. The forces are here referred to as: small i.e $1 \cdot 10^{-7}$ AU/day^2, which corresponds to the average value in the solar system, medium i.e $5 \cdot 10^{-7}$ AU/day^2, which is five times larger than the solar system value and large i.e $1 \cdot 10^{-6}$ AU/day^2, 10 times larger than the outgassing in our solar system.

Finally, the mass loss rate as well as the sublimation rate was calculated using Equations (1.9) and (1.11) together with the estimated values A_1, A_2 and A_3 constants, as well as the estimated activity function $g(r)$. Assuming a spherical body with a diameter of 5 km consisting of water ice grazing the star, undergoing sublimation as a result ejecting some of its mass. The collimation efficiency factor of the ejected material was estimated to $\kappa = 0.8$ and the temperature of the emitted gas was estimated to be the equilibrium temperature, see Equation (1.6) at the distance of the icy body. It was assumed that the material undergoing sublimation was water ice with density 1000 kg/m^3 (Hui & Jewitt 2017).

Chapter 3

Results and Discussion

3.1 N-body Simulations

Results from simulating the system over 20 million years with 5000 test particles can be found in Figure 3.1, where the initial position of each test particle is plotted together with the branching ratios of the particles fates at the end of the simulation. Note that this simulation was nearly equivalent to the one done by Rodet & Lai (2023), but with more detailed branching ratios, the simulation time was also longer and significantly more particles were included, 20 thousand instead of 1000.

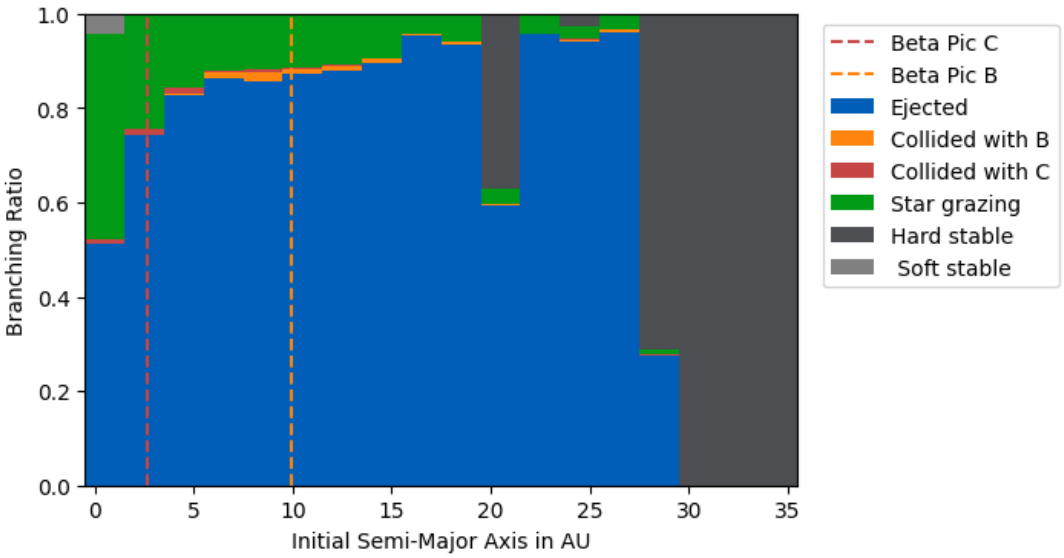

Figure 3.1: The result of a 20 million year long simulation of 20 thousand test particles. The initial distance from the star of each particle is shown together with the branching ratio of final fates of the particles. Positions of the planets (β Pic c and β Pic b) are marked with vertical dashed lines.

In Figure 3.1, stable regions are found near 20 AU and beyond 27 AU. This is similar

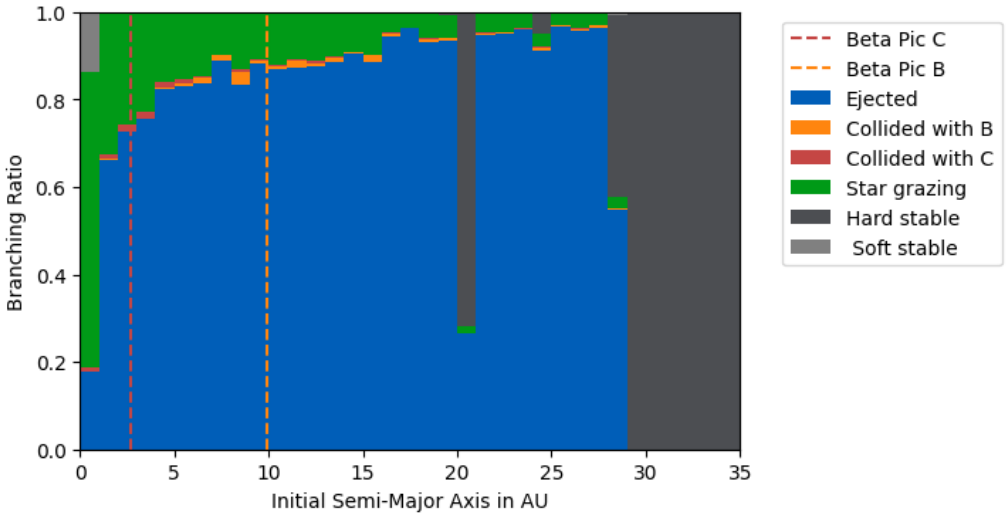

Figure 3.2: The result of a 20 million year long simulation of 20 thousand test particles. The bin size has been reduced to 1 AU.

to the result obtained by Rodet & Lai (2023). The major difference is that Rodet & Lai (2023) find a wider stability region that starts at 25 AU. The differences between Figure 3.1 and the results obtained by Rodet & Lai (2023) could depend on several things. The values for the stellar and planetary parameters used by Rodet & Lai (2023) are different from the ones used in this work as they are based on different sources. The planetary parameters are not known with a high precision therefore it is a large source of uncertainty in simulating the system. For example, as seen in Table 1.2, the mass of the β Pic b is known with an uncertainty of several Jupiter masses. The mass is a quantity that is of most importance for N-body simulations and thus has a significant effect on the outcome of the simulations. Even though different planetary parameters were used, the results obtained here are similar to the results obtained by Rodet & Lai (2023), compare Figure 1.5 with Figure 3.1, thus the results can be considered robust in general.

An effective parallelization of the simulation made the inclusion of 20 thousand particles possible as several smaller simulations could be run on several different cores simultaneously, shortening the total simulation time. The simulation speed was also improved through avoiding saving and checking lists of removed particles when integrating. The inclusion of a larger amount of test particles in the simulations allows for a more statistically significant result. The more particles included, the more accurate the branching ratios will be, and so it can be justified to decrease the bin size from 2 AU (Figure 3.1) to 1 AU (Figure 3.2). Figure 3.2 is more detailed and some features become clearer than in Figure 3.1. The stable region at 20 AU is narrower and deeper, meaning that a higher percentage of particles seeded in that region remain on stable orbits. It could be possible due to mean-motion orbital resonance with one of the planets, most likely β Pic b.

The stable regions found here are not exactly aligned with the planetesimal rings observed by Okamoto et al. (2004) at 6.4, 16 and 30 AU. The hard-stable regions at 20 AU and beyond 27 AU as seen in Figure 3.1 could be compared to the 16 and 30 AU rings inferred by Okamoto et al. (2004). The results of this project do not predict that a stable planetesimal ring could be sustained in the proximity of 6.4 AU. The simulations done by Rodet & Lai (2023) find only one stable region beyond 25 AU and thus only match one of the rings, at 30 AU, observed by Okamoto et al. (2004). The James-Webb space telescope will in the future observe the system at infrared wavelengths and may provide more constraints on the nature of the 6.4 AU ring, and confirm or rule out the previous observations (Chen et al. 2023).

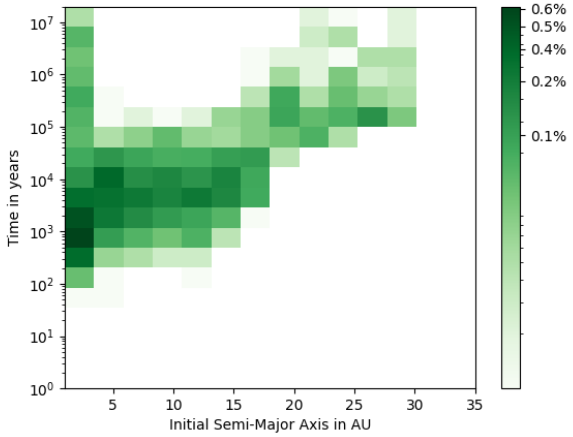

(a) Percentage of the total amount of test particles that are star-grazing at different times plotted against their initial semi-major axis.

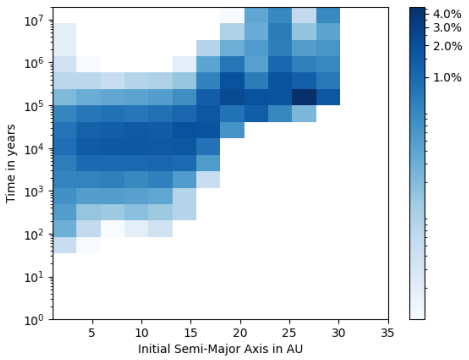

(b) Percentage of total amount of particles that are ejected at different times.

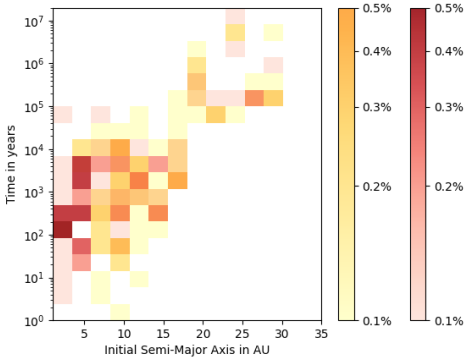

(c) Percentage of total amount of particles that are colliding different times.

Figure 3.3: Percentages of star-grazing (a), ejected (b) and collided (c) particles. In figure (c), test particles colliding with planet b are indicated with orange (left colorbar) and test particles colliding with planet c are indicated with red (right colorbar).

About 21 % of the total number of the simulated test particles survive the simulations

without being ejected, star-grazing or colliding with a planet. These particles are the so-called stable particles. The majority of the stable test particles are also hard stable, meaning that they do not stray far from their initial orbits. Thus, planetesimal reservoirs could survive in the stable 20 AU and >27 AU regions. The soft stable test particles with initial semi-major axes of about 1 AU are either on chaotic orbits or have migrated to somewhere in the system, likely one of the two hard stable regions. It can be assumed that the > 27 AU stable region is extending for all larger distances.

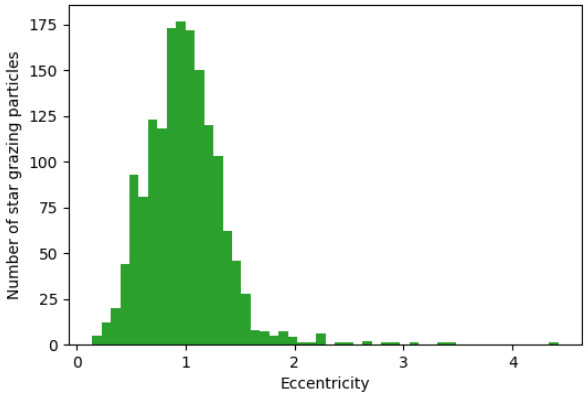

Figure 3.4: The distribution of eccentricities saved for particles labeled as star-grazers.

The results show that approximately 8 % of all test particles placed in the simulation become star-grazers, the majority of them coming form the inner regions of the system, see Figure 3.1. Figure 3.3a shows how large of a percentage out of all test particles become star-grazing as a function of time and as a function of their initial semi-major axis. A trend can be observed: particles in the inner system seem to become star-grazers earlier on than in the outer system. The simulation implies that at an age equal to the current age of the β Pic system, star-grazers are sourced from the >27 AU region. These are mostly on hard-stable orbits, but interactions with the planets are capable of converting these particles into star-grazers on 20-million year timescales. The orbital elements of star-grazers were saved before removal of the particle from the simulation, the distribution of the eccentricities of star-grazing test particles can be found in Figure 3.4. The distribution seems to be centered at $e = 1$, indicating that the majority of particles that become star-grazing do so on highly eccentric or hyperbolic orbits.

Similarly, test particles originating from the inner parts of the system seem to become ejected earlier than the particles originating in outer parts of the system. A trend similar to the one in Figure 3.3a can be seen in Figure 3.3b where the percentage of ejections per time and initial semi-major axis is shown. Ejection is the most common outcome for test particles placed in the simulation, approximately 70 % of all test particles become ejected from the system. Ejection is a dominating fate for particles seeded on all semi-major axes, except the stable regions and the region closest to the star, between 1 and 3 AU. There, particles star-graze more intensely in the early years of the simulations and thus star-grazing and ejection are equally likely in that region, see Figure 3.1. In the

region very closest to the star that is only resolvable in Figure 3.2, star-grazers dominate over ejections. The particles that are this close to the star are strongly affected by the gravitation of it and less so by the planets, it could explain this result.

A small percentage of the test particles collide with a planet, see Figure 3.1. Rodet & Lai (2023) present a similarly distribution of collisions. The small amount of collisions might be due to the inclinations of the test particles. Test particles on an orbit that is inclined with respect to the orbit of the planets are less likely to collide with any of the planets and thus the amount of colliding particles is roughly 1 %. Test particles with small initial semi-major axes are more likely to collide with β Pic c as the planet is on an orbit with a low semi-major axis of 2.68 AU. Similarly, test particles with higher initial semi-major axes are more likely to collide with β Pic b as it is located at 9.93 AU. The results seem to agree with this reasoning. Collisions seem to on average happen earlier on in the systems lifetime, in contrast to ejections and star-grazings they start to happen at a time scale of hundreds of years. Later the collision timescales seem to follow the same pattern as ejections and star-grazings, see Figure 3.3c.

3.2 Outgassing Force

The result of the two-body simulations where only the star and a test particle were included are presented in Figure 3.5. Force was applied in all three directions, see Figure 2.2, and it was expected to affect the orbit of the test particles in three different directions, corresponding to the three components. One of the force components is acting in $\boldsymbol{t}_t$, the anti-parallel direction of the transversal velocity of the particle, thus slowing it down by an amount of Δv per unit of time.

For an elliptic orbit, when a force acts on the particle unevenly throughout its orbit. The eccentricity of the orbit is expected to change. For very eccentric orbits, the difference between apoastron and periastron is large and since the outgassing force is dependent on the distance to the star it means that the force will be much larger at periastron than at apoastron. As a consequence, the particles velocity change Δv will be greater in periastron, working against the increase in velocity that happens at periastron in an elliptical orbit. This will lead to a shrinking of the orbit, a new apoastron and periastron will form at shorter distances to the star, see Figure 3.6. Due to the imbalance of the force, the periastron distance will decrease slower than the apoastron distance. The force at the shorter apoastron will be greater than before, this is also true for the periastron however since the apoastron distance shortens faster, the force will also grow faster. The orbit will continue to shrink unevenly due to the force imbalance, however as the orbit shrinks the difference between the forces will become smaller, until they become equally big. This happens when apoastron and periastron are at equal distances from the star and thus by definition the orbit is circular with an eccentricity of $e = 0$, see Figure 3.6.

The slow down that is caused by the component anti-parallel to the transversal velocity of the particle decreases the energy of the particle, pushing it closer to the star. Thus a particle affected by the outgassing force will spiral into the star. If the initial orbit of the test particle is circular, it is expected to remain circular in the spiral whereas if the initial

orbit is elliptic it is expected to circularise. In simulations where the initial eccentricity of the particle was set to $e = 0$, the applied force resulted in a decrease in semi-major axis however not in either the inclination nor the eccentricity, see Figure 3.5a. As expected, the particle is spiraling toward the star, eventually colliding with it, without changing the orbital eccentricity.

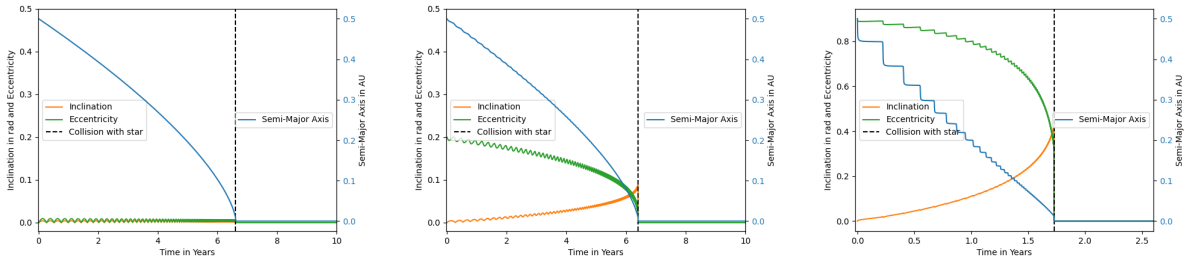

(a) $e = 0$ (b) $e = 0.2$ (c) $e = 0.9$

Figure 3.5: Outgassing force was applied to test particles at placed at $a = 0.5$ AU with an inclination of $i = 0°$. The initial eccentricity of the test particle was varied, firstly 0, then 0.2 and finally 0.9. Note that the limits on the axes are not the same for all plots, as the collision with star happens earlier for higher eccentricities.

The circularisation effect can be seen in results of test particles on an orbit with some initial eccentricity larger than zero. For the case of low eccentricity $e = 0.2$ see Figure 3.5b, the eccentricity diminished at an increasing rate, eventually approaching 0 as a approached zero. So the closer the particle was to the planet, the more circular its orbit was. The eccentricity change of the test particle with initial eccentricity of $e = 0.9$, see Figure 3.5c, follows a similar pattern. Its eccentricity also decreased rapidly and converges to 0 as a goes to zero. The higher initial eccentricity has made the process go faster. This is expected, as for orbits with higher eccentricities the force difference between apoastron and periastron is larger.

The second component of the force acts in the direction of the angular momentum, perpendicular to the orbital plane in $\boldsymbol{t}_n$ see Figure 2.2. Thus it will have an effect on the tilt of the orbit, the inclination. Depending on the direction of the force, the inclination might increase or decrease due to this component of the outgassing force. In Figures 3.5b and 3.5c the initial inclination grows, since A_2 was set to a positive value. Note that for $e = 0$ the inclination does not grow, it remains at $i = 0$, see Figure 3.5a. This is due to the same reason as mentioned above for eccentricity. When in a circular orbit, all points in the orbit are at equal distance from the star, meaning that the force acts symmetrically on all of them. In an elliptic orbit, the force will act unevenly in the orbit, resulting in a tilt. The final component of the outgassing force is the radial component acting in $\boldsymbol{t}_r$, see Figure 2.2. When applied, it produces periodic variation the semi-major axis and eccentricity of the test particle The higher the magnitude of the component the larger the variations. The mean values of the semi-major axis and eccentricity do not change due to the force in the radial direction. Note that the change in orbital parameters is higher than what is observed for some comets in our solar system. This is due to the fact

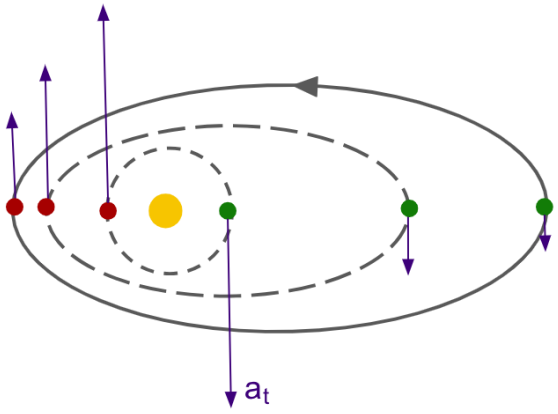

Figure 3.6: Circularisation of an elliptical orbit. The initial orbit is shown with the solid gray line, periastron is marked with the red dot and apoastron with green. The normal component of the outgassing acceleration is marked with the purple arrow, pointing in the direction anti-parallel to the direction of the transversal velocity.

that many of them are on larger orbits than modeled here as well as the fact that β Pic is more massive and hotter than the Sun, see Table 1.1.

The results from simulations including the outgassing force and the two planets of the system can be found in Figure 3.7. In this work, the outgassing acceleration was included for particles that were identified as star-grazers in the large-scale N-body simulations, see Section 3.1. The force was applied on three test particles with different orbital parameters representative of the results obtained in the 20 million year N-body simulations, see Figure 3.4. The non-gravitational force was applied in three different strengths that will from now on be referred to as small i.e $A_i = 10^{-7}$ AU/day^2, medium i.e $A_i = 5 \cdot 10^{-7}$ AU/day^2 and large i.e $A_i = 10^{-6}$ AU/day^2 where $i = 1, 2, 3$. A_1, A_2 and A_3 are the constants that define the strength of the non-gravitational acceleration, see Equation (1.7). Note that for our model the values of A_1, A_2 and A_3 are here assumed to be equal which is not necessarily true for observed objects (Hui & Jewitt 2017).

In sub-figures 3.7a, 3.7b and 3.7c the results of simulations with particle 1 (P1) are shown. The results of simulations with particle 2 (P2) are shown in sub-figures 3.7d, 3.7e and 3.7f. Lastly for results of simulations with particle 3 (P3), see sub-figures 3.7g, 3.7h and 3.7i. Note that in all the sub-figures in Figure 3.7 the scale on the x-axis varies, as the test particles collide with the star at different times depending on the initial orbit and the magnitude of the applied force. Note that in Figure 3.7 the inclination in radians and eccentricity is plotted on the left x-axis and the semi-major axis in AU is plotted on the right x-axis.

Figures 3.7a and 3.7d look similar to the figures produced for a theoretical, eccentric star-grazing particle where only the star is included, see Figure 3.5c. Also see Figure 3.8 for the trajectory of Particle 1 and compare to Figure 3.6. Note that the figure does not show the change in inclination. In Figures 3.7b and 3.7c as well as 3.7e and 3.7f, the

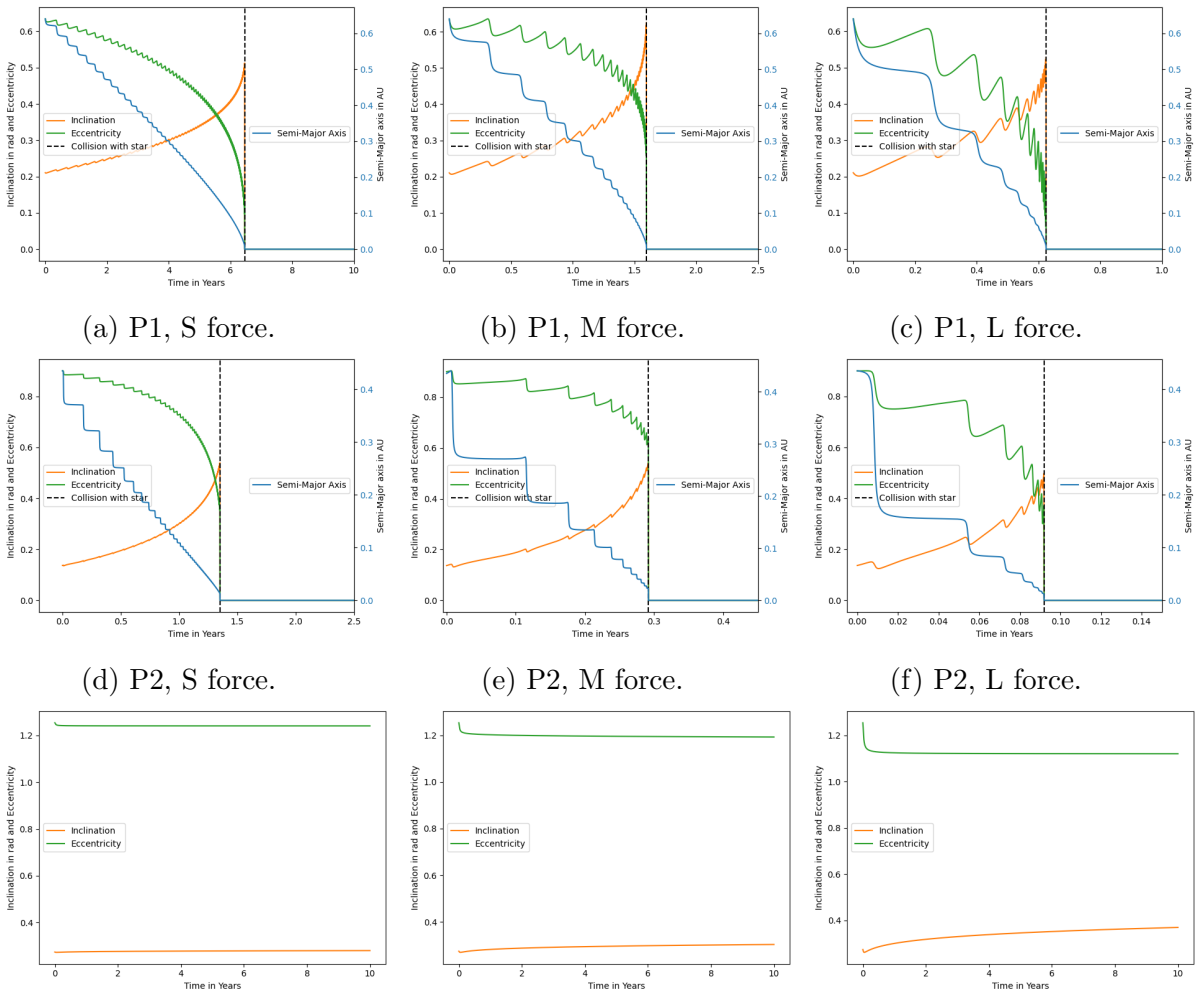

(a) P1, S force. (b) P1, M force. (c) P1, L force.

(d) P2, S force. (e) P2, M force. (f) P2, L force.

(g) P3, S force. (h) P3, M force. (i) P3, L force.

Figure 3.7: Results from N-body simulations of the β Pic system performed with three different test particles on different orbits. Each row corresponds to a test particle, Particle 1 is shown in the uppermost row, followed by Particle 2 and finally Particle 3 furthest down. The non-gravitational acceleration due to outgassing was included and varied in strength. Each column corresponds to a strength of the acceleration, lowest to the left and highest to the right.

collision with the star happens fast and the shape of the curves look different due to the small time before collision. It can still be determined that for the two first test particles that were simulated, P1 and P2, the results are similar to the results obtained for a theoretical test particle above, see Figure 3.5. This means that the star-grazers produced in the N-body simulation of the β Pic system, see Section 3.1, behave as predicted after the outgassing force is applied to them. It also seems as if the gravitational force from the two planets of the system do not affect the test particle while it outgasses.

The third particle included in these simulations, see sub-figures 3.7g, 3.7h and 3.7i, was on a hyperbolic initial orbit meaning that it had a high initial velocity and it was not

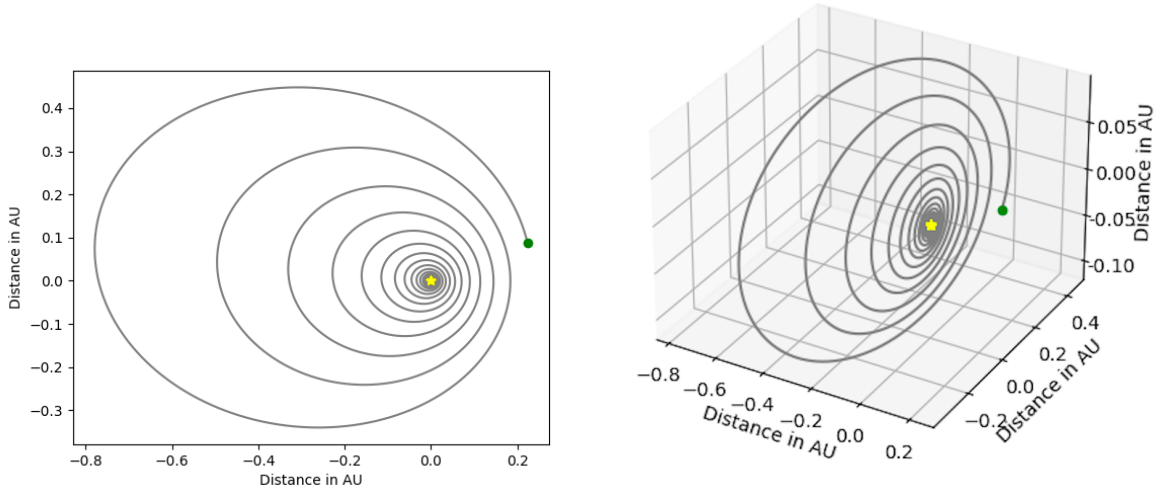

(a) x and y directions.

(b) x, y and z directions.

Figure 3.8: Trajectory of particle 1 with initial orbital parameters $[e, a, i]_{P1}$ = [0.63,0.64 AU, 0.21 rad] affected by a large-sized outgassing acceleration of 10^{-6} AU/day^2. Compare with Figure 3.6. Note that (a) does not include the inclination, (b) does. The green dot is the position at which the particle was initiated in the simulation.

gravitationally bound to the star even though it was passing close by to it. As can be seen in Figures 3.7g, 3.7h and 3.7i, none of the outgassing forces applied are not enough for the test particle to get captured by the star. Note that for hyperbolic orbits, i.e when $e > 1$, the semi-major axis depends on the distance between the branches of the hyperbola and cannot be interpreted as a scale of distance to the star anymore as a particle in hyperbolic orbit is not bound to the star. In Rebound, $a < 0$ for $e > 1$. It is not relevant to track negative semi-major axes for this study as it does not contribute to the understanding of ougassing. In Figures 3.7g, 3.7h and 3.7i the a was only plotted when $e < 1$, since the particle was never trapped, a was never positive and it is thus not plotted .

We have here only modeled outgassing for particles that are located within 0.3 AU of the star. The sublimation limit for the β Pic system was determined to be at 10.0 ± 0.2 AU using Equation 1.8, see Section 2.2, meaning that outgassing of water starts at much larger distances than what was modeled here. With the above examples we have also shown that that the ougassing can change the orbit of test particles significantly. A particle affected by the non-gravitational acceleration might thus not even end up in the star-grazing orbits that we base the simulations on, if the outgassing force is already strong at larger orbital distances. In order to improve the model, future work should include the ougassisng force at larger distances from the star.

Finally, the mass loss, of the particles during the simulations are shown in Figure 3.9. It was estimated using Equation (1.9), see Section 2.2. The same three particles from the outgassing simulations were studied, under the same small, medium and large forces. For

all the particles the mass decreases with time due to the sublimation as expected and the mass loss is highly dependent on the magnitude of the force, see Figure 3.9. Masses of the particles decrease unequally fast, due to the difference in the position of the particles, as the temperature decreases with stellar distance d, see Figure 3.9. Particles 1 and 2 distances to the star d_1 and d_2 decrease due to the the non-gravitational force as seen in results above, see Figure 3.7. Initially P1 is further away from the star than P2 $d_2 < d_1$. As time progresses d_2 decreases while d_1 increases. The difference in direction of the position are due to where in the orbit the particle is initiated, i.e its phase shift. Particle 1 has passed its periastron and moves toward the apoastrion and moving away from the star, even though its semi-major axis is reduced. It results in a less steep mass loss over time. Particle 2 on the other hand is moving toward its periastron and its position d_2 decreases over time. The mass loss of P2 resembles that as the particle looses more mass per day as time progresses, see Figure 3.9. For the third particle, on an initially hyperbolic orbit, the mass loss was studied during its close-encounter with the star as the outgassing was not strong enough to capture it, see Figure 3.7. Particle 3 is initially further away from the star than P1 and P2. Its orbital velocity is also greater than for the two particles, meaning that its distance d_3 to the star does not decrease equally much due to the force. For the case of the small force, its mass does not diminish during the close-encounter with the star, and instead stagnates at around 200 Pg (10^{12}kg), see sub-figure 3.9a, note that in this figure the x-limit has been set for illustrative purposes, as the particle did continue at approximately this mass for the rest of the simulation (10 years). For the large force, it does not seem to survive this close encounter, as its mass diminishes before leaving the proximity of the star, see Figure 3.9. Since it is moving with a high velocity, the distance d_3 is not as affected by the outgassing and is approximately constant, see sub-figure 3.9f resulting in a linear decrease in mass as can be seen in Figure 3.9e, here as well as for the medium force, the mass of P3 diminishes during the close-encounter.

The results indicate that icy comets can survive on star-grazing orbits for time scales of a couple of days, depending on their initial orbits. Note that the mass loss estimations are based on water ice. Sublimated gas from FEBs have been observed in Ca and Fe, implying that the bodies are likely consisting of metals. As we know a portion of the star-grazers likely originate from stable regions in the outer system, we conclude that they are icy before grazing the star. The ice is most probably sublimated before the comets reach 0.3 AU, where they are observed as FEBs, and are at that point active asteroids. Our simulations therefore indirectly assume that the outgassing force is generated by outgassing of dust, rather than water. But because of the usage of the Marsden et al. (1973) formalism, the results are insensitive to this difference. Models of the sublimation process can also be constructed based on the material properties of the evaporating material (see e.g. Kimura et al. (2002)), but we chose to approach this problem from the direction of the change in orbital elements (Marsden et al. 1973) because this is closest to the observed quantities in the system.

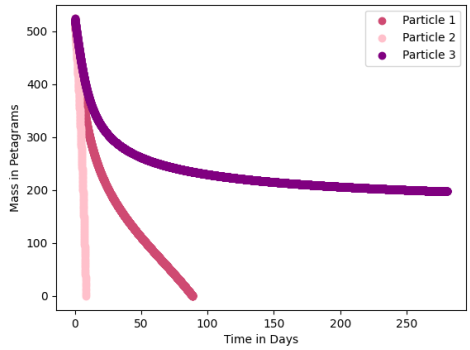

(a) The estimated mass loss, S force.

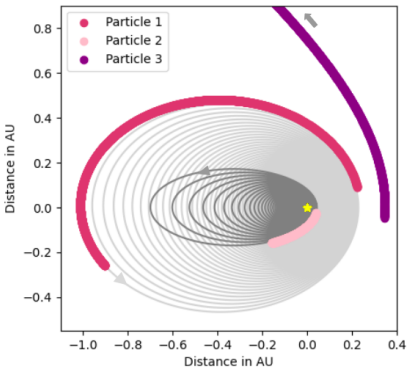

(b) Orbital trajectories, S force.

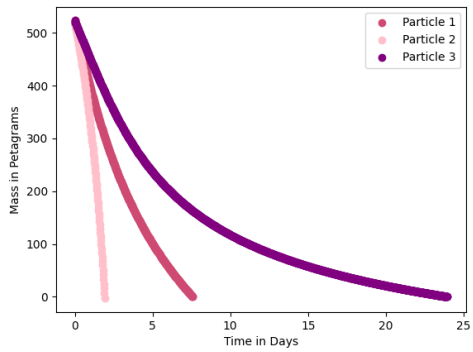

(c) The estimated mass loss, M force.

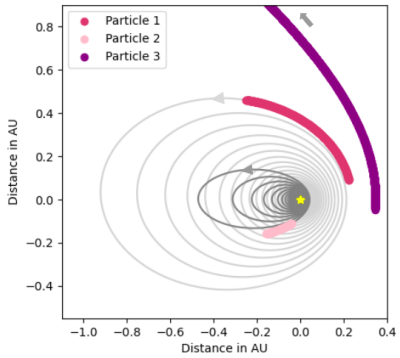

(d) Orbital trajectories, M force.

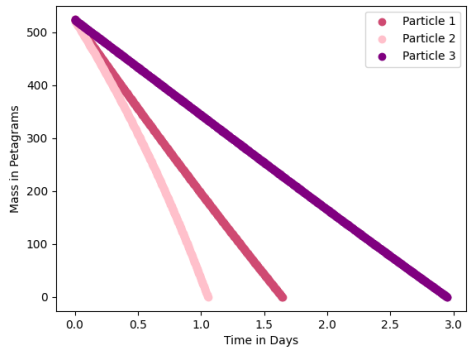

(e) The estimated mass loss, L force.

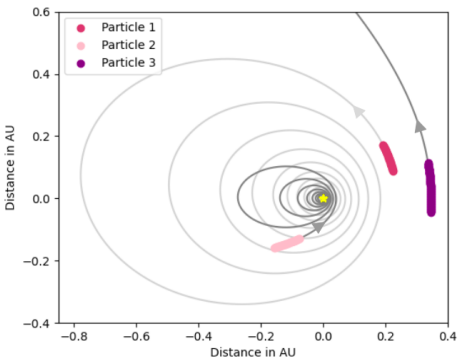

(f) Orbital trajectories, L force.

Figure 3.9: Mass loss and orbital trajectories of particles 1, 2 and 3 with the following sets of orbital parameters: $[e, a, i]_{P1}$ = [0.63,0.64 AU, 0.21 rad], $[e, a, i]_{P2}$ = [0.91, 0.44 AU, 0.14 rad] and $[e, a, i]_{P3}$ = [1.25, -1.36 AU, 0.27 rad]. The particles were assumed to be spheres of water ice with a diameter of 5 km. In sub-figures (b), (d) and (f) gray lines indicate the total predicted trajectories and arrows indicate the direction of motion of the particles. In sub-figures (a), (c) and (e) the scale on the y-axis is in petagrams, that is equivalent to 10^{12} kg. Also note that the (a), (b) and (d) hade custom limited axis for illustrative purposes due to large distances of P3.

Chapter 4

Conclusions

It can be concluded that the β Pictoris system is capable of hosting a stable planetesimal belt at a distance greater than 27 AU from the star for millions of years until its current age of 23 Myr. In this region it is possible for planetesimals to not become ejected nor collide with any of the planets. N-body simulations of the system show that test particles seeded in that region stay in their orbits, deviating only a maximum of 5 % from their initial semi-major axis at any time of the simulation. The simulations also show that star-grazers are being formed in this region of stability after tens of millions of years and from that it can be concluded that such a planetesimal belt could still produce infalling objects today. It is in contrast to Rodet & Lai (2023) that find that the FEBs observed today would need to be formed by collisions of objects in the planetesimal belt. This could explain the variable absorption observations reported in the system by among others Beust et al. (1989) and Kiefer et al. (2014). Through this conclusion it can be inferred that the planetesimals that fall into the star are icy comets that start to sublimate at the stellar distance of approximately 10 AU and that more detailed treatment of sublimation physics is needed even for particles relatively far out, much more distant than the 0.3 AU limit assumed in this study. On top of the stability region at 30 AU, the results show evidence that a stable planetesimal belt is possible at 20 AU, roughly consistent with observations by Okamoto et al. (2004). Test particles originating within this region may also become star-grazing at a time-scale of 20 million years. It could thus be argued that if a planetesimal belt exists at the distance of 20 AU, it could also be a source of FEBs.

From studying the time at which particles become star-grazing it can be concluded that particles do star-graze from the stable regions mentioned above at time scales of 20 million years, corresponding of the age of the β Pictoris system. The difference in results could be explained by the different times of integration, Rodet & Lai (2023) only perform simulations for half of the systems age. In this study, 20 times more particles were included, making the results more statistically accurate. It was possible due to an effective parallelization of the simulation as well as an implementation that makes more efficient use of searching and saving of output. The simulations show that test particles collide with both planets at time scales of 10-20 million years, meaning that their temperatures and compositions could possibly be affected by collisions with comets. N-body simu-

lations performed here can also be used in order to study the moon-formation of the planets, it was however outside the scope of this work.

From simulations including the non-gravitational outgassing acceleration on test particles on different orbits it can be concluded that particles affected by outgassing fall into the star if the outgassing works against the motion of the particle. Outgassing in the direction of motion has been observed in our solar system (Hui & Jewitt 2017) however it was not included in this study. The elliptic orbits of test particles become circularized as the semi-major axis decreases. Furthermore, from modeling of the outgassing of test particles, the mass loss over time could be estimated. We predict that the time icy comets can spend in their star-grazing strongly depends on the magnitude of the ougassing force, for particles on very eccentric orbits this time could be as low as a couple of days. The assumptions of the non-gravitational acceleration made in this work are based on empirical observations of the solar system. The adaptation of them on the β Pictoris system is a great approximation as the star is hotter, larger and more massive than the Sun. The outgassing acceleration could be measured in the β Pic system through precise observations of the ongoing sublimation of exocomets. Another assumption made in this study is that the star-grazing bodies are made up out of water ice. The sublimation of Ca and Fe has been observed for the FEBs in the system, meaning that the bodies are most likely metallic and if they contained any water, it is likely that it has evaporated earlier in the journey from the stable regions in the outer system. It can also be concluded that the large scale N-body simulations would yield different results if the outgassing force was included, as it has been proven to affect the trajectories of the test particles.

Bibliography

Aumann, H. H. (1985), 'Iras observations of matter around nearby stars.', *Publications of the Astronomical Society of the Pacific* **97**, 885–891.

Beust, H., Lagrange-Henri, A., Vidal-Madjar, A. & Ferlet, R. (1989), 'The beta pictoris circumstellar disk. ix-theoretical results on the infall velocities of ca ii, al iii, and mg ii', *Astronomy and Astrophysics* **223**, 304–312.

Beust, H. & Morbidelli, A. (1996), 'Mean-motion resonances as a source for infalling comets toward β pictoris', *Icarus* **120**(2), 358–370.

Beust, H. & Morbidelli, A. (2000), 'Falling Evaporating Bodies as a Clue to Outline the Structure of the β Pictoris Young Planetary System', *Icarus* **143**(1), 170–188.

Chen, C., Sargent, B., Sloan, G., Hines, D. C. & Nickson, B. (2023), Thermal emission spectroscopy of beta pictoris' prototypical debris disk.

Crifo, F., Vidal-Madjar, A., Lallement, R., Ferlet, R. & Gerbaldi, M. (1997), 'β Pictoris revisited by Hipparcos. Star properties.', *A&A* **320**, L29–L32.

Currie, T., Burrows, A., Madhusudhan, N., Fukagawa, M., Girard, J. H., Dawson, R., Murray-Clay, R., Kenyon, S., Kuchner, M., Matsumura, S., Jayawardhana, R., Chambers, J. & Bromley, B. (2013), 'A combined VLT and Gemini Study of the atmosphere of the directly-imaged planet, beta pictoris b', *The Astrophysical Journal* **776**(1), 15.

Deeg, H. J. & Alonso, R. (2018), Transit Photometry as an Exoplanet Discovery Method, *in* H. J. Deeg & J. A. Belmonte, eds, 'Handbook of Exoplanets', Springer International Publishing, p. 633–657.

European Southern Observatory (2008), 'Beta pictoris as seen in infrared light'. Accessed: 2023-12-15.
URL: *https://www.eso.org/public/images/eso0842a/*

Fitzsimmons, A., Meech, K., Matrà, L. & Pfalzner, S. (2023), 'Interstellar Objects and Exocomets', *arXiv e-prints* .

Gray, R. O., Corbally, C. J., Garrison, R. F., McFadden, M. T., Bubar, E. J., McGahee, C. E., O'Donoghue, A. A. & Knox, E. R. (2006), 'Contributions to the nearby stars (NStars) project: Spectroscopy of stars earlier than m0 within 40 pc–the southern sample', *The Astronomical Journal* **132**(1), 161–170.

Hui, M.-T. & Jewitt, D. (2017), 'Non-gravitational Acceleration of the Active Asteroids', *AJ* **153**(2), 80.

Karttunen, H., Kröger, P., Oja, H., Poutanen, M. & Donner, K. J. (2016), *Fundamental astronomy*, 6 edn, Springer.

Kennedy, G. M. (2018), 'Exocomet orbit fitting: accelerating coma absorption during transits of β Pictoris', *MNRAS* **479**(2), 1997–2006.

Kenworthy, M. A., Mellon, S. N., Bailey, J. I., Stuik, R., Dorval, P., Talens, G. J. J., Crawford, S. R., Mamajek, E. E., Laginja, I., Ireland, M., Lomberg, B., Kuhn, R. B., Snellen, I., Zwintz, K., Kuschnig, R., Kennedy, G. M., Abe, L., Agabi, A., Mekarnia, D., Guillot, T., Schmider, F., Stee, P., de Pra, Y., Buttu, M., Crouzet, N., Kalas, P., Wang, J. J., Stevenson, K., de Mooij, E., Lagrange, A. M., Lacour, S., Lecavelier des Etangs, A., Nowak, M., Strøm, P. A., Hui, Z. & Wang, L. (2021), 'The β Pictoris b Hill sphere transit campaign. I. Photometric limits to dust and rings', *A&A* **648**, A15.

Kiefer, F., Lecavelier des Etangs, A., Boissier, J., Vidal-Madjar, A., Beust, H., Lagrange, A. M., Hébrard, G. & Ferlet, R. (2014), 'Two families of exocomets in the β Pictoris system', *Nature* **514**(7523), 462–464.

Kimura, H., Mann, I., Biesecker, D. A. & Jessberger, E. K. (2002), 'Dust Grains in the Comae and Tails of Sungrazing Comets: Modeling of Their Mineralogical and Morphological Properties', *Icarus* **159**(2), 529–541.

Kitchin, C. R. (1995), *Optical Astronomical Spectroscopy*, Inst. of Physics Publ.

Lacour, S., Wang, J. J., Rodet, L., Nowak, M., Shangguan, J., Beust, H., Lagrange, A. M. & Abuter, R. e. a. (2021), 'The mass of β Pictoris c from β Pictoris b orbital motion', *A&A* **654**, L2.

Lagrange, A. M. (2014), 'Direct imaging of exoplanets', *Philosophical Transactions of the Royal Society of London Series A* **372**(2014), 20130090.

Lagrange, A.-M., Bonnefoy, M., Chauvin, G., Apai, D., Ehrenreich, D., Boccaletti, A., Gratadour, D., Rouan, D., Mouillet, D., Lacour, S. & Kasper, M. (2010), 'A giant planet imaged in the disk of the young star β pictoris', *Science* **329**(5987), 57–59.

Lagrange, A. M., Gratadour, D., Chauvin, G., Fusco, T., Ehrenreich, D., Mouillet, D., Rousset, G., Rouan, D., Allard, F., Gendron, É., Charton, J., Mugnier, L., Rabou, P., Montri, J. & Lacombe, F. (2009), 'A probable giant planet imaged in the β Pictoris disk. VLT/NaCo deep L'-band imaging', *A&A* **493**(2), L21–L25.

Lagrange, A. M., Meunier, N., Rubini, P., Keppler, M., Galland, F., Chapellier, E., Michel, E., Balona, L., Beust, H., Guillot, T., Grandjean, A., Borgniet, S., Mékarnia, D., Wilson, P. A., Kiefer, F., Bonnefoy, M., Lillo-Box, J., Pantoja, B., Jones, M., Iglesias, D. P., Rodet, L., Diaz, M., Zapata, A., Abe, L. & Schmider, F.-X. (2019), 'Evidence for an additional planet in the β Pictoris system', *Nature Astronomy* **3**, 1135–1142.

Mamajek, E. E. & Bell, C. P. M. (2014), 'On the age of the β pictoris moving group', *Monthly Notices of the Royal Astronomical Society* **445**(3), 2169–2180.

Marsden, B. G., Sekanina, Z. & Yeomans, D. K. (1973), 'Comets and nongravitational forces. V', *AJ* **78**, 211.

Martin, R. G. & Livio, M. (2012), 'On the evolution of the snow line in protoplanetary discs', *MNRAS* **425**(1), L6–L9.

Mayor, M., Pepe, F., Queloz, D., Bouchy, F., Rupprecht, G., Lo Curto, G., Avila, G., Benz, W., Bertaux, J. L., Bonfils, X., Dall, T., Dekker, H., Delabre, B., Eckert, W., Fleury, M., Gilliotte, A., Gojak, D., Guzman, J. C., Kohler, D., Lizon, J. L., Longinotti, A., Lovis, C., Megevand, D., Pasquini, L., Reyes, J., Sivan, J. P., Sosnowska, D., Soto, R., Udry, S., van Kesteren, A., Weber, L. & Weilenmann, U. (2003), 'Setting New Standards with HARPS', *The Messenger* **114**, 20–24.

Micheli, M., Farnocchia, D., Meech, K. J., Buie, M. W., Hainaut, O. R., Prialnik, D., Schörghofer, N., Weaver, H. A., Chodas, P. W., Kleyna, J. T., Weryk, R., Wainscoat, R. J., Ebeling, H., Keane, J. V., Chambers, K. C., Koschny, D. & Petropoulos, A. E. (2018), 'Non-gravitational acceleration in the trajectory of 1I/2017 U1 ('Oumuamua)', *Nature* **559**, 223–226.

Murray, C. D. & Dermott, S. F. (1999), *Solar system dynamics*, Cambridge University Press.

Nowak, M., Lacour, S. & Lagrange, A. M. e. a. (2020), 'Direct confirmation of the radial-velocity planet β Pictoris c', *A&A* **642**, L2.

Okamoto, Y. K., Kataza, H., Honda, M., Yamashita, T., Onaka, T., Watanabe, J.-i., Miyata, T., Sako, S., Fujiyoshi, T. & Sakon, I. (2004), 'An early extrasolar planetary system revealed by planetesimal belts in β Pictoris', *Nature* **431**(7009), 660–663.

Quirrenbach, A. (2022), 'The Equilibrium Temperature of Planets on Eccentric Orbits: Time Scales and Averages', *Research Notes of the American Astronomical Society* **6**(3), 56.

Rein, H. & Liu, S. F. (2012), 'REBOUND: an open-source multi-purpose N-body code for collisional dynamics', *A&A* **537**, A128.

Rein, H. & Spiegel, D. S. (2015), 'IAS15: a fast, adaptive, high-order integrator for gravitational dynamics, accurate to machine precision over a billion orbits', *MNRAS* **446**(2), 1424–1437.

Rodet, L. & Lai, D. (2023), 'Planet-Driven Scatterings of Planetesimals Into a Star: Probability, Timescale and Applications', *arXiv e-prints* p. arXiv:2308.10326.

Smith, B. A. & Terrile, R. J. (1984), 'A circumstellar disk around β pictoris', *Science* **226**(4681), 1421–1424.

Swamy, K. (1997), *Physics of comets*, World scientific.

Veras, D., Eggl, S. & Gänsicke, B. T. (2015), 'Sublimation-induced orbital perturbations of extrasolar active asteroids and comets: application to white dwarf systems', *MNRAS* **452**(2), 1945–1957.

Welsh, B. Y. & Montgomery, S. (2016), 'Exocomet Circumstellar Fe I Absorption in the Beta Pictoris Gas Disk', *Publications of the Astronomical Society of the Pacific* **128**(964), 064201.

Wilner, D. J., Andrews, S. M. & Hughes, A. M. (2011), 'Millimeter Imaging of the β Pictoris Debris Disk: Evidence for a Planetesimal Belt', *ApJ* **727**(2), L42.

Wright, J. T. (2018), Radial Velocities as an Exoplanet Discovery Method, *in* H. J. Deeg & J. A. Belmonte, eds, 'Handbook of Exoplanets', Springer International Publishing, p. 619–631.

Zieba, S., Zwintz, K., Kenworthy, M. A. & Kennedy, G. M. (2019), 'Transiting exocomets detected in broadband light by TESS in the β Pictoris system', *A&A* **625**, L13.

Appendix A

Report

FYSB06 - Physics - Applied Wrok

Exocomets in the beta Pictoris system

Author
Klaudia Jaworska

Supervisor
Jens Hoeijmakers

LUNDS UNIVERSITET

July 7th, 2023

Introduction

Beta Pictoris is a young planetary system that consists of an A-type star of 8000 K temperature, a debris disk and two known planets. [1] The system has been observed rigorously over the last decade. Irregular spectroscopic features have been observed calcified as Falling Evaporating Bodies (FEBs) or in other words, exocomets. The density of the FEBs is high in the system, with several hundreds absorption features observed every year. The observations done over the last decade show that the vast majority of the FEBs are red-shifted. [2]

In systems constructed like β Pic, comets and other minor bodies are expected. Observations have shown that debris disks in systems like this commonly have asymmetric formations caused by the gravitational perturbations of planets in the system. The high dominance of red-shifted features can also be explained by the dynamics caused by the two planets of the system. [3] FEBs bear with them information about the formation and evolution of the stellar system, thus there is a high significance in their studies. They can also be used to understand the dynamics of the system, the behavior of FEBs in the β Pic system was an indicator to the presence of the second planet discovered within the system, Beta Pic c. [2]

The radial velocity, v_r of an object moving in a Keplerian orbit is given by:

$$v_r(t) = \frac{2\pi}{P} \frac{a_s \sin(i)}{\sqrt{1-\epsilon^2}} \left(\epsilon \cos(\omega) + \cos(\omega + \phi(t))\right), \tag{A.1}$$

where P is the orbital period, a_s is the semi major axis, i is the inclination of the orbit, ϵ the eccentricity, ω the argument of periapsis and ϕ the true anomaly. [4] The equilibrium temperature T_{eq} of a body in a solar system can be found using:

$$T_{eq} = T_\star \left(\frac{(1-A)R_\star^2}{4a_s^2} \right)^{1/4}, \tag{A.2}$$

where $T_\star$ is the temperature of the star and $R_\star$ is the radius of the star. A is the albedo of the body. [7]

Method

The analysis was done on spectra taken by the HARPS spectrograph. The set consisted of 9100 exposures where the stellar spectrum was captured in the wavelength range of 378 nm - 691 nm. [5] The spectra were interpolated, normalized and translated to velocity space with the stellar radial velocity as zero-point. Then, they were examined for absorption features at some velocity with respect to the star. Absorption lines of particular interest were FeI and CaII. The CaIIK and CaIIH lines were found to be active and several red-shifted absorption features were found in the wavelength region of them. Two absorption features stood out on the nights of 2019-12-11 and 2019-12-12, as they were blue-shifted and accelerated toward the stellar CaII lines. These were

investigated further by orbit fitting. A Gaussian fit was performed on the absorption over the exposures of interest, and the center wavelengths were plotted against time. Equation (A) was then fit to the data using the high performance array computing program JAX. [6] Note that as the system is transiting, the inclination was assumed to be 90 °. Some of the data points were removed due to their large error, thus the fit was only performed on a portion of the data. When the orbits were known, the equillibrium temperatures of the objects were calculated using Equation (A), the albedo was assumed to be zero.

Results

An accelerating CaII absorption feature was discovered on the night of 2019-12-11. A similar feature was also observed the night after, 2019-12-12. Both features are blue-shifted and accelerate toward the stellar absorption line, see Figure A.1.

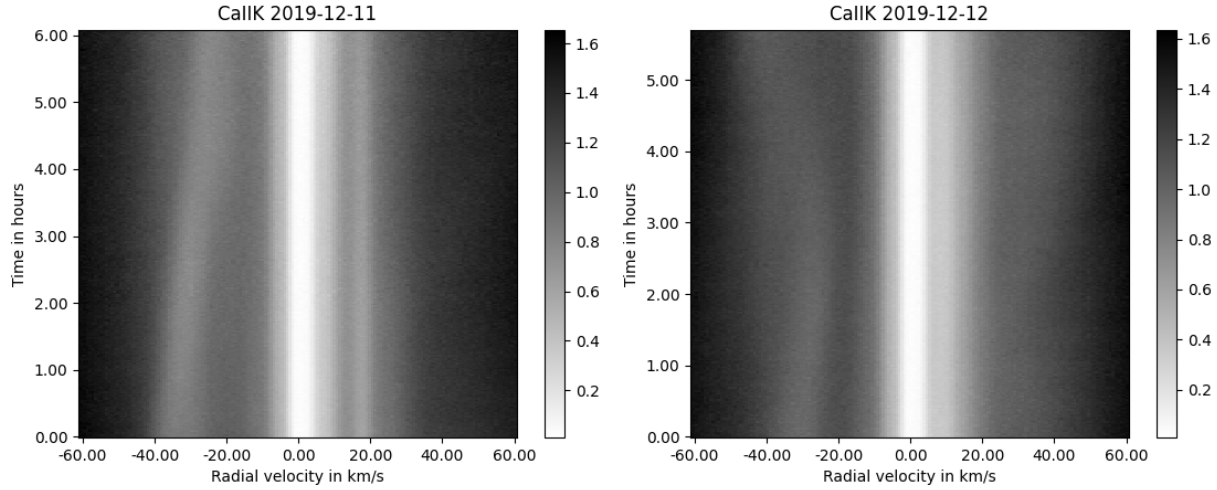

(a) 2019-12-11 (b) 2019-12-12

Figure A.1: Blue-shifted accelerating absorption features of CaII on the nights of 2019-12-11 and 2019-12-12. Note that CaIIK is displayed in the figures, the same absorption feature appears in CaIIH, displayed in Figure A.6 in Appendix A.

The result from orbit fittings done on the absorption spectra in Figure A.1a and Figure A.1b can be seen in Figure A.2 and Figure A.3 respectively. The median orbit parameters together with their errors are presented in Figure A.2 and Figure A.3. Figure A.4 shows the data and the fits that are plotted in red, showing the match between the data and the fit. As can be seen from Figure A.4, the data from the first night is has a lower error and the fit is more accurate than for the second night. Note that in the figures show only a portion of the data, as the fit was not done on all data points from the nights.

The resulting orbital parameters are shown in Figure A.2 and Figure A.3. Note that in the figure, the orbital period P and the center transit time $T0$ are given in seconds s and the argument of petastrion ω is given in degrees °. The final periods of both the features observed on 2019-12-11 and 2019-12-12 were found to be approximately 9.2 days.

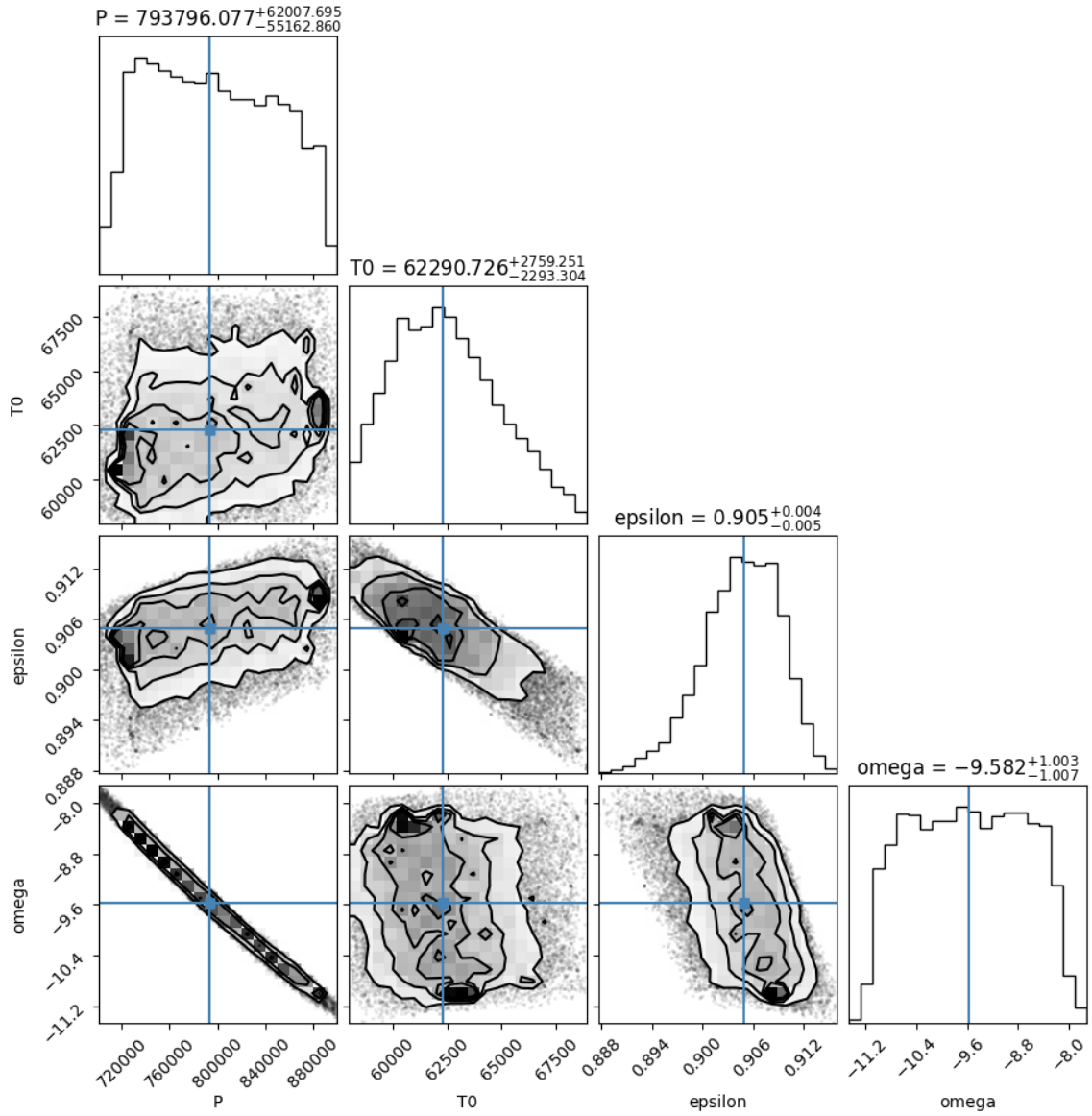

Figure A.2: Posteriors resulting from fitting Equation (A) to absorption data from 2019-12-11. Note that P and $T0$ are here in seconds s and ω in degrees °.

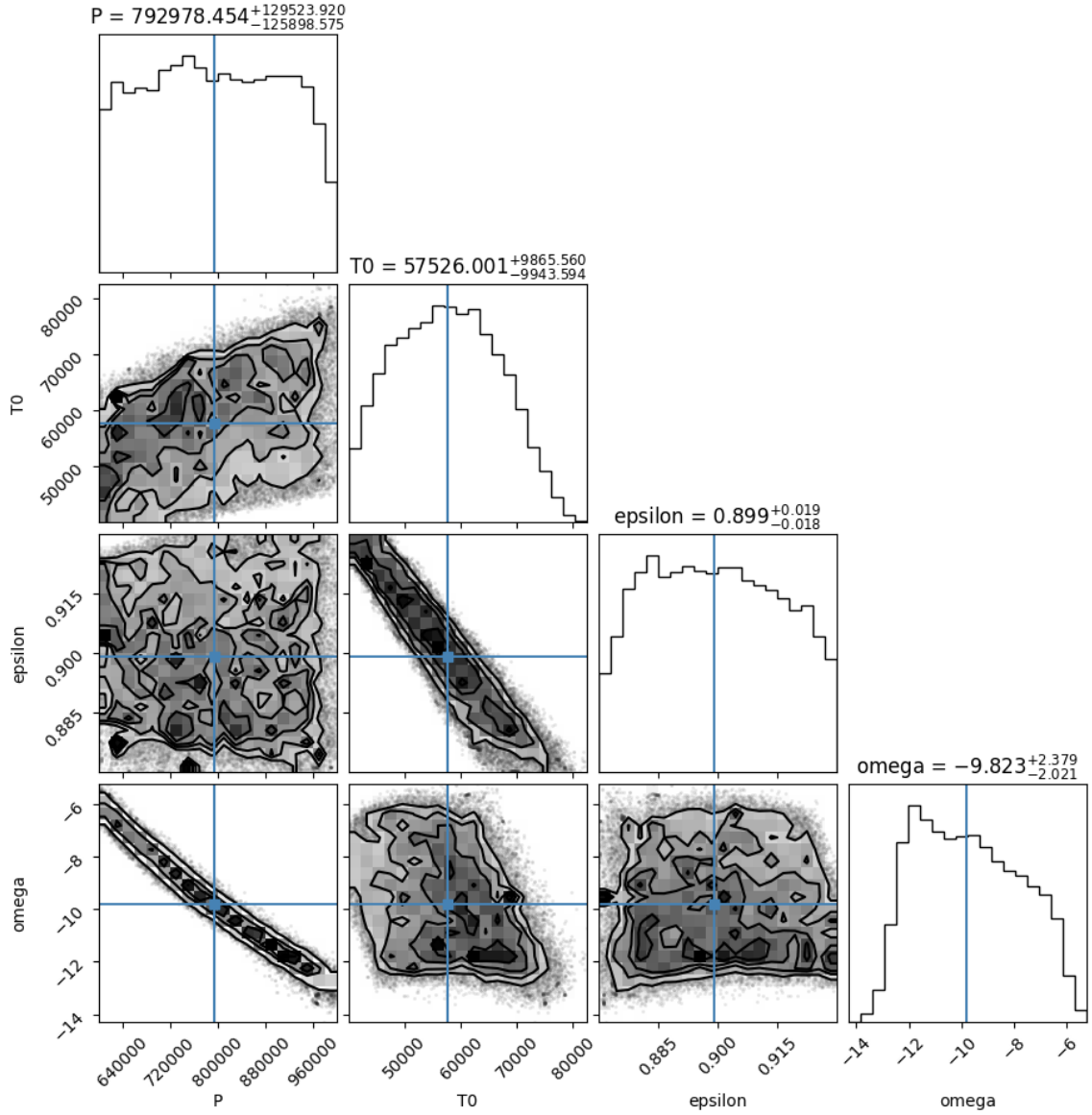

Figure A.3: Posteriors resulting from fitting Equation (A) to abosorption data from 2019-12-12.Note that P and $T0$ are here in seconds s and ω in degrees $^\circ$.

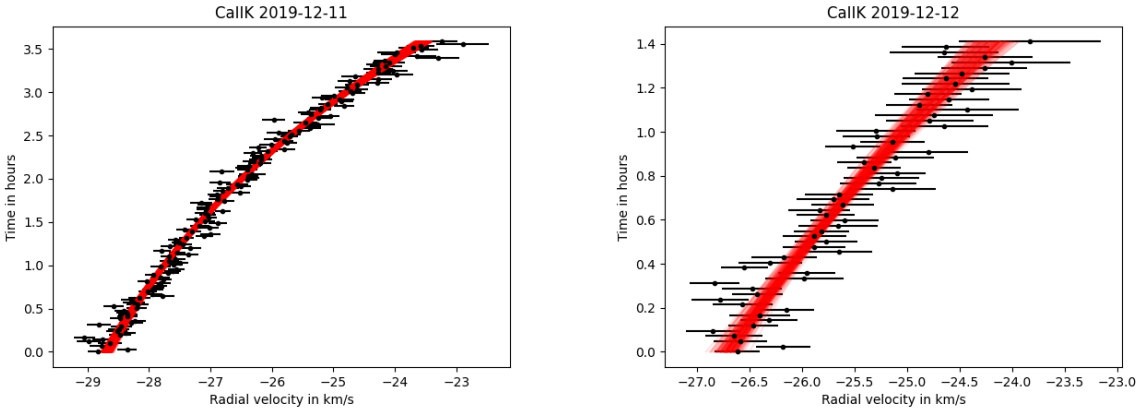

(a) 2019-12-11 (b) 2019-12-12

Figure A.4: The center wavelengths of the absorption plotted against time. JAX fit plotted in red over the data.

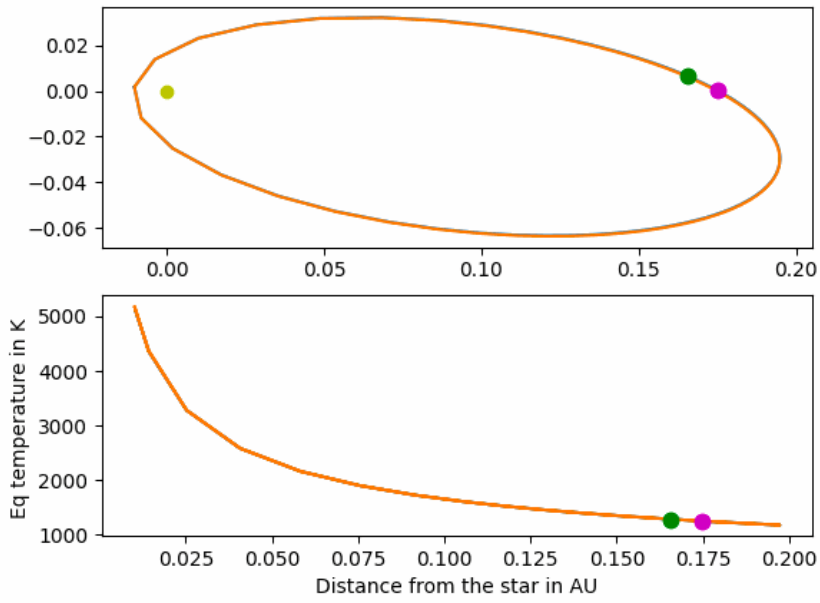

Figure A.5: The orbits of the two objects observed are plotted in the upper panel. The pink dot represents the 2019-12-11 object and the green represents the 2019-12-12 object. In the lower panel, the equilibrium temperature of the objects is plotted. Note that the orbits are so similar to each other that they are plotted on top of one another. The yellow dot is representing the star.

Finally, Figure A.5 shows the orbits and the temperature experienced by the bodies plotted. Note that due to the similarity of the orbits they are plotted on top of one

another. Figure A.5 shows that the lowest temperature the objects experience is 1173 K and the highest 5112 K, thus they most likely are made up of metals and are asteroids.

Conclusions

In conclusion, two absorption features have been discovered. They do not appear to be from the same object. In fact trough fitting a Keplerian orbit to each of the absorption spectra in question, it was found that the absorptions are on approximately the same orbit as can be seen in Figure A.5, but they are a day apart thus indicating on a relation between the two absorptions. The absorption features could belong to two asteroids who once were one larger body broken apart by the tidal force in their orbit. The orbits of the asteroids allow for estimations of the temperature experienced by the bodies. The highest temperature the asteroids experience is approximately 5000 K.

References

[1] *The Extrasolar Planets Encyclopaedia* [Internet] [Cited 2023 June 9] Available from: https://exoplanet.eu/home/

[2] Rebollido, I., et al. *Exocomets: A spectroscopic survey.* Astronomy and Astrophysics 639 (2020): A11. Available from:https://arxiv.org/abs/2003.11084

[3] Beust, H. *Exocomets, minor bodies and resonant phenomena in debris disks.* SF2A-2022: Proceedings of the Annual meeting of the French Society of Astronomy and Astrophysics. Available from: https://ui.adsabs.harvard.edu/abs/2022sf2a.conf..297B/abstract

[4] Quanz, S. P., *Extrasolar Planets.* ETH Zurich Institut for Particle Physics and Astrophysics. 2017-02-18

[5] Mayor, M., et al. *Setting New Standards with HARPS* . The Messenger (ISSN0722-6691), No.114. December 2003. Available from: https://ui.adsabs.harvard.edu/abs/2003Msngr.114...20M/abstract

[6] *JAX: High-Performance Array Computing* [Internet] [Cited 2023 July 95] Available from: https://jax.readthedocs.io/en/latest/

[7] Quirrenbach, A. *The Equilibrium Temperature of Planets on Eccentric Orbits: Time Scales and Aver- ages* . American Astronomical Society 6 56. March 2022. Available from: https://iopscience.iop.org/article/10.3847/2515-5172/ac5f0d

Appendix A: CaIIH

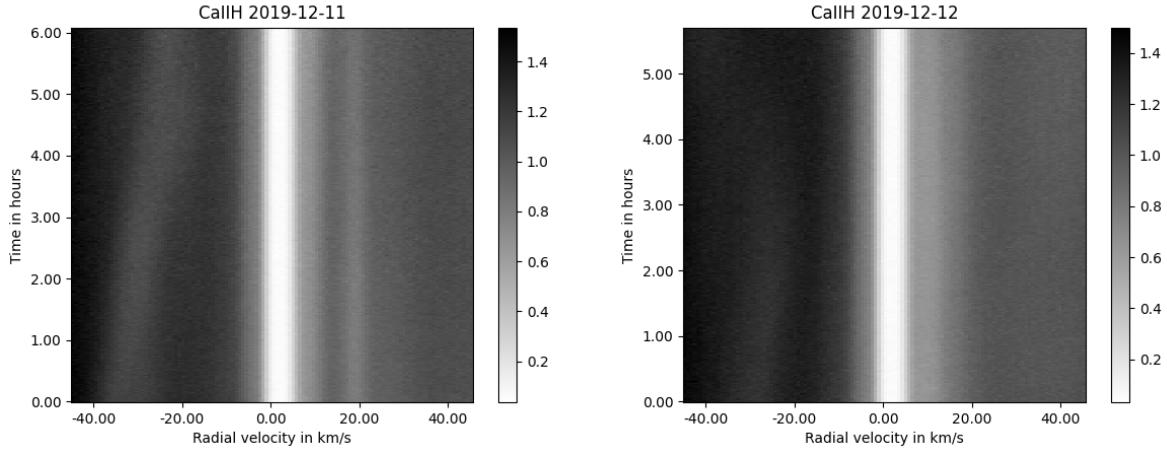

(a) (b)

Figure A.6: Blue-shifted accelerating absorption features of CaII on the nights of 2019-12-11 and 2019-12-12. Note that CaIIH is displayed here. For the same absorption feature but in CaIIK, see Figure A.1.